nature metabolism

ARTICLES

https://doi.org/10.1038/s42255-020-00311-5

Check for updates

The PI3K pathway preserves metabolic health through MARCO-dependent lipid uptake by adipose tissue macrophages

Julia S. Brunner[1,2,16], Andrea Vogel[1,2,16], Alexander Lercher[3], Michael Caldera[3,13], Ana Korosec[4], Marlene Pühringer[1,2], Melanie Hofmann[1,2], Alexander Hajto[1,2], Markus Kieler[1,2], Lucia Quemada Garrido[1,2], Martina Kerndl[1,2], Mario Kuttke[1,2], Ildiko Mesteri[5], Maria W. Górna[6], Marta Kulik[6], Paulina M. Dominiak[6], Amanda E. Brandon[7,8], Emma Estevez[9], Casey L. Egan[9,14], Florian Gruber[10], Martina Schweiger[11], Jörg Menche[3,13], Andreas Bergthaler[3], Thomas Weichhart[12], Kristaps Klavins[3,15], Mark A. Febbraio[9,14], Omar Sharif[1,2,17] ✉ and Gernot Schabbauer[1,2,17] ✉

Adipose tissue macrophages (ATMs) display tremendous heterogeneity depending on signals in their local microenvironment and contribute to the pathogenesis of obesity. The phosphoinositide 3-kinase (PI3K) signalling pathway, antagonized by the phosphatase and tensin homologue (PTEN), is important for metabolic responses to obesity. We hypothesized that fluctuations in macrophage-intrinsic PI3K activity via PTEN could alter the trajectory of metabolic disease by driving distinct ATM populations. Using mice harbouring macrophage-specific PTEN deletion or bone marrow chimeras carrying additional PTEN copies, we demonstrate that sustained PI3K activity in macrophages preserves metabolic health in obesity by preventing lipotoxicity. Myeloid PI3K signalling promotes a beneficial ATM population characterized by lipid uptake, catabolism and high expression of the scavenger macrophage receptor with collagenous structure (MARCO). Dual MARCO and myeloid PTEN deficiencies prevent the generation of lipid-buffering ATMs, reversing the beneficial actions of elevated myeloid PI3K activity in metabolic disease. Thus, macrophage-intrinsic PI3K signalling boosts metabolic health by driving ATM programmes associated with MARCO-dependent lipid uptake.

Obesity is a serious public health burden and risk factor for metabolic syndrome and co-morbidities, including type 2 diabetes and cardiovascular and fatty liver diseases. Excessive lipid accumulation in white adipose tissue (WAT) leads to pathological expansion associated with adipocyte hypertrophy and ensuing inefficient lipid storage. Consequently, lipids accumulate in peripheral tissues, instigating lipotoxic insults including insulin resistance, apoptosis and inflammation[1].

Obesity promotes immune cell infiltration of WAT, characterized by the accumulation of ATMs[2]. While the contribution of ATMs to systemic metabolically triggered inflammation in obesity is established[3–5], recent work demonstrates their extensive plasticity, heterogeneity and diversity[3,6–8]. In obesity, subsets of ATMs adopt a metabolic activation state linked to prominent lysosomal and phagocytic activity[6,9,10]. Beneficial functions associated with WAT remodelling, including the clearance of dying adipocytes and lipid droplets, have been ascribed to distinct metabolically activated ATM populations[6,11,12]. The surrounding adipose microenvironment and its multiple fluctuating stimuli during disease progression have emerged as influencers of ATM plasticity and function[8,9,11,13]. Akin to ATMs, bone marrow-derived macrophages that differentiate in the presence of adipose tissue exhibit neutral lipid accumulation, lysosomal biogenesis and upregulation of their lipid and general metabolism[10,14,15]. Despite this progress, large gaps in knowledge remain. In particular, the signalling pathways and triggers governing ATM heterogeneity that may drive or protect against obesity-instigated metabolic derangements remain unknown.

[1]Institute for Vascular Biology, Center for Physiology and Pharmacology, Medical University Vienna, Vienna, Austria. [2]Christian Doppler Laboratory for Arginine Metabolism in Rheumatoid Arthritis and Multiple Sclerosis, Vienna, Austria. [3]CeMM Research Center for Molecular Medicine of the Austrian Academy of Sciences, Vienna, Austria. [4]Skin and Endothelium Research Division, Department of Dermatology, Medical University of Vienna, Vienna, Austria. [5]Institute of Pathology Überlingen, Überlingen, Germany. [6]Biological and Chemical Research Centre, Department of Chemistry, University of Warsaw, Warsaw, Poland. [7]Insulin Action and Energy Metabolism Laboratory, Division of Diabetes & Metabolism, Garvan Institute of Medical Research, Darlinghurst, New South Wales, Australia. [8]Faculty of Medicine and Health, School of Medical Sciences, University of Sydney, Sydney, New South Wales, Australia. [9]Cellular & Molecular Metabolism Laboratory, Division of Diabetes & Metabolism, Garvan Institute of Medical Research, Darlinghurst, New South Wales, Australia. [10]Research Division of Biology and Pathobiology of the Skin, Department of Dermatology, Medical University of Vienna, Vienna, Austria. [11]Institute of Molecular Biosciences, University of Graz, Graz, Austria. [12]Center of Pathobiochemistry and Genetics, Institute of Medical Genetics, Medical University of Vienna, Vienna, Austria. [13]Present address: Max Perutz Laboratories, Vienna, Austria. [14]Present address: Drug Discovery Biology, Monash Institute of Pharmaceutical Sciences, Monash University, Parkville, Victoria, Australia. [15]Present address: Rudolfs Cimdins Riga Biomaterials Innovations and Development Centre, Riga Technical University, Riga, Latvia. [16]These authors contributed equally: Julia S. Brunner, Andrea Vogel. [17]These authors jointly supervised this work: Omar Sharif, Gernot Schabbauer. ✉e-mail: omar.sharif@meduniwien.ac.at; gernot.schabbauer@meduniwien.ac.at

Lipid storage in adipose tissue, muscle and liver is promoted by pro-lipogenic and anti-lipolytic insulin action[16]. PI3K signalling and its downstream effectors, including protein kinase B (AKT), are pivotal for the metabolic and mitogenic effects of insulin[16]. PI3K activity is tightly regulated with several negative feedback loops maintaining its homeostasis, including termination by PTEN[16]. Indeed, hallmark phenotypes of mice with deletions or mutations in various PI3K isoforms include growth retardation and insulin resistance[17–19]. Further, despite increases in adiposity and hepatic steatosis after conditional PTEN deletion in adipocytes or hepatocytes, respectively, these animals exhibit improved glucose tolerance and insulin sensitivity[20,21]. Similarly, beneficial metabolic health after caloric excess as a consequence of improved insulin-induced PI3K signalling occurs in animals with conditional PTEN loss in pancreatic beta cells and muscle[22,23].

Here, we hypothesized a central role for myeloid-cell-intrinsic PI3K signalling in influencing metabolic disease by impacting ATM plasticity through environmental signals from metabolically stressed adipose tissue. We identify that PI3K signalling sustains a disease-sparing ATM population responsible for lipid scavenging and catabolism, assigning a key role for the scavenger receptor MARCO herein. Thus, we provide insight into how macrophage-intrinsic PI3K activity protects against lipotoxic responses, which may have important implications for wide-ranging metabolic diseases.

Results

Myeloid-cell-intrinsic PI3K dictates metabolic health under nutrient excess. To understand if adipose tissue-derived signals modulate the PI3K–AKT pathway in macrophages, we first subjected C57BL/6J mice to different treatments including short-term high fat diet (ST-HFD), long-term high fat diet (HFD) or acute lipolysis induced by the β3-adrenoceptor agonist CL316,243 and evaluated macrophage AKT phosphorylation (p-AKT). Like many macrophages, murine ATMs express the cell surface antigens F4/80 and CD11b. While both ST-HFD and CL316,243 did not impact circulating insulin levels, consistent with previous studies, the resulting disruption of adipose tissue homeostasis was linked to F4/80^{+}CD11b^{+} (FB) macrophage infiltration[24,25] (Extended Data Fig. 1a,b). Compared to animals fed a normal diet (ND), long-term (16 weeks) HFD-fed animals exhibited hyperinsulinaemia and FB macrophage infiltration within adipose tissue (Extended Data Fig. 1a,b). All treatments caused substantial p-AKT loss within FB macrophages (Extended Data Fig. 1c). Investigating potential links to metabolically stressed adipose tissue, we next stimulated primary peritoneal macrophages with adipocyte conditioned media (ACM) from epididymal WAT (eWAT) of HFD-fed animals. ACM treatment also ablated macrophage p-AKT (Extended Data Fig. 1d). As limited PI3K signalling is associated with insulin resistance in metabolic tissues[17–19], we hypothesized that perturbing myeloid-cell-intrinsic PI3K changes the trajectory of metabolic disease.

To examine if limited myeloid PI3K signalling affects metabolic health in obesity, we next utilized transgenic mice overexpressing PTEN ($Pten^{Tg/+}$). These animals are protected from diet-induced-obesity-associated insulin resistance partly by their increased energy expenditure[26]. To circumvent the impacts of non-hematopoietic PTEN overexpression and associated reported growth retardation[26], we performed bone marrow transplantation (BMT) of hematopoietic cells from $Pten^{Tg/+}$ or wild-type (WT) littermates into WT animals (Fig. 1a). PTEN overexpression and concomitant limited PI3K signalling was observed in adaptive immune and monocytic cells from the blood of $Pten^{Tg/+}$ animals versus controls (Fig. 1b and Extended Data Fig. 2a). In contrast to the results in whole-body transgenic animals[26], following BMT, there were no differences in weight, lean or fat mass after a HFD (Extended Data Fig. 2b). Hyperinsulinaemic-euglycaemic clamps revealed unremarkable effects of hematopoietic PTEN overexpression ($Pten^{Tg/+}$>WT) on insulin sensitivity as glucose infusion rates required to maintain euglycaemia were similar in $Pten^{Tg/+}$ animals versus controls ($Pten^{+/+}$>WT; Extended Data Fig. 2c). Confirming this observation, there was equivalent glucose disposal and suppression of hepatic glucose output (Extended Data Fig. 2d). Strikingly, while minimal effects on glucose tolerance between groups occurred during ND feeding, HFD-fed $Pten^{Tg/+}$>WT mice exhibited glucose intolerance versus $Pten^{+/+}$>WT controls (Fig. 1c). This was associated with lower serum insulin levels after glucose gavage, suggestive of impaired insulin secretion (Fig. 1d). Concordantly, HFD-fed $Pten^{Tg/+}$>WT mice exhibited lower C-peptide levels (Fig. 1e). Decreased insulin secretion after glucose gavage of $Pten^{Tg/+}$>WT mice was not associated with augmented pancreatic CD68 expression, thus suggesting that increased CD68^{+} pancreatic macrophages, pivotal for pancreatic beta cell lipotoxicity and inflammation, are unlikely to be involved[27,28] (Extended Data Fig. 2e). In an independent BMT cohort, we observed elevated serum triglycerides in HFD-fed $Pten^{Tg/+}$>WT mice, disconnected from accelerated weight gain, indicative of disturbances in lipid metabolism (Fig. 1f and Extended Data Fig. 2f). Furthermore, as compared to controls, obese $Pten^{Tg/+}$>WT animals displayed increased liver weights and clear tendencies towards increased hepatic steatosis (Fig. 1g,h). These effects were independent of augmented hepatic transcription of key lipogenic mediators, suggesting increased hepatic de novo lipogenesis was not responsible for the elevated hepatic steatosis of HFD-fed $Pten^{Tg/+}$>WT mice. In fact, while no differences were observed for *Ppar-γ* and *Srebf1*, obese $Pten^{Tg/+}$>WT animals exhibited attenuated hepatic *Fasn*, *Acaca* and *Acacb* expression (Fig. 1i), possibly explained by decreased insulin-stimulated induction[29]. While expected increases in PTEN expression in ATMs of $Pten^{Tg/+}$>WT HFD-fed animals compared to controls was evident, their pro-inflammatory cytokine transcription was not augmented (Fig. 1j). Together, these observations indicate that lower PI3K activity in hematopoietic cells aggravates metabolic dysfunction in obesity independently of ATM-instigated inflammation.

We next examined if augmenting myeloid-cell PI3K activity, facilitated through myeloid *LysM*-Cre-specific PTEN deletion ($Pten^{\Delta myel}$)[30], prevented deleterious effects of obesity. PTEN deletion and accompanying augmented PI3K signalling were detected specifically in blood monocytes of $Pten^{\Delta myel}$ animals but not controls (Fig. 2a and Extended Data Fig. 3a). While no differences in glucose tolerance occurred during ND feeding, HFD-fed $Pten^{\Delta myel}$ animals displayed improved glucose tolerance, independent of serum insulin differences, compared to that in $Pten^{WT}$ littermates (Extended Data Fig. 3b,c). HFD-fed $Pten^{\Delta myel}$ animals further displayed improved insulin sensitivity, a phenotype requiring metabolic stress as it was absent during ND feeding (Fig. 2b).

We noticed, on average, HFD-fed $Pten^{\Delta myel}$ mice were unable to reach the same adiposity as their co-housed WT littermates (Fig. 2c). We therefore stratified animals into high- (HW) and low- (LW) weight gainers to abolish weight and fat mass differences, ensuring testing for weight-independent metabolic effects (Fig. 2d and Extended Data Fig. 3d). The LW gainer phenotype after HFD feeding was genotype independent and became apparent at 12 weeks, and LW gainers did not display genotype-specific insulin sensitivity differences (Extended Data Fig. 3d,e). Importantly, stratification nullified weight differences in obese HW gainers, revealing that augmenting myeloid PI3K exerted protective effects on metabolic health independently of weight (Extended Data Fig. 3e).

In contrast to the enhanced hepatic steatosis of $Pten^{Tg/+}$>WT chimeric mice, HW-gaining $Pten^{\Delta myel}$ mice were protected from liver steatosis and exhibited lower liver damage as evaluated by serum indicators of hepatotoxicity, including alanine transaminase and aspartate transaminase (Fig. 2e,f and Extended Data Fig. 3f). Decreased hepatic steatosis of HFD-fed $Pten^{\Delta myel}$ animals was not coupled to hepatic lipogenic transcriptional differences (Fig. 2g).

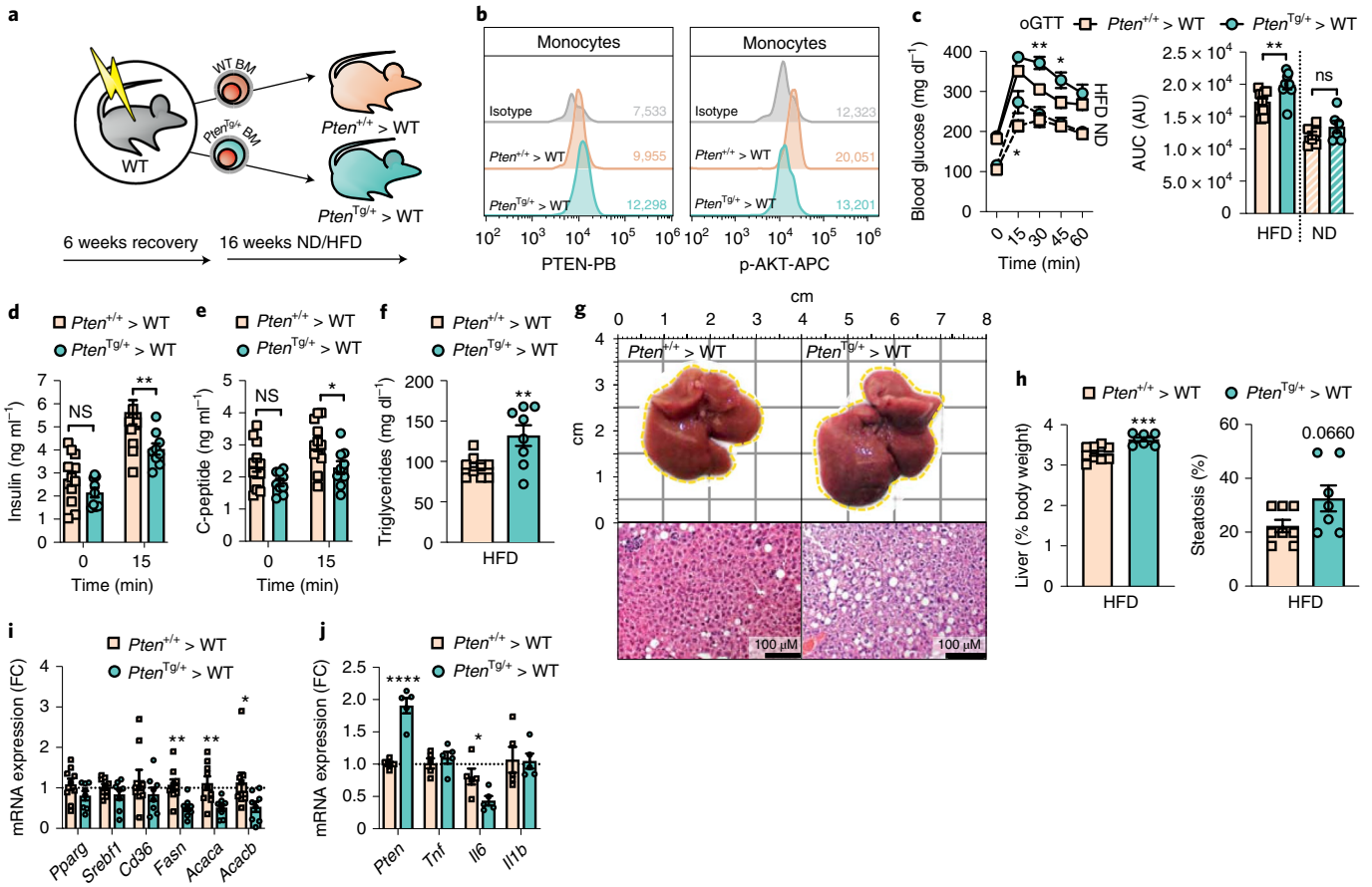

Fig. 1 | Limiting PI3K signalling via PTEN overexpression in hematopoietic/myeloid cells worsens metabolic health in obesity. a, WT mice were lethally irradiated and transplanted with WT (*Pten*$^{+/+}$> WT) or PTEN-transgenic (*Pten*$^{Tg/+}$> WT) bone marrow. Following a 6-week recovery period on a chow diet (ND), mice were fed a HFD. **b**, Histograms depicting PTEN and p-AKT expression in blood monocytes from WT or *Pten*$^{Tg/+}$ animals. Cells were gated on CD45$^+$CD11b$^+$CD3$^-$B220$^-$Ly6G$^-$Ly6C$^+$. **c**, Oral glucose tolerance test (oGTT) and area under the curve (AUC) of *Pten*$^{+/+}$> WT ($n=6$ ND; $n=12$ HFD) or *Pten*$^{Tg/+}$> WT ($n=6$ ND; $n=9$ HFD) mice, 16 weeks after feeding (**$P=0.0042$ and *$P=0.0242$, two-way ANOVA of HFD groups with Bonferroni's correction; *$P=0.0355$, two-way ANOVA of ND groups with Bonferroni's correction; **$P=0.0051$ for AUC; two-tailed Student's *t*-test). **d**,**e**, Plasma insulin (**d**) and C-peptide (**e**) levels of HFD-fed animals shown in **c** (**$P=0.0095$ and *$P=0.0248$, two-way ANOVA with Bonferroni's correction). **f**, Serum triglycerides of *Pten*$^{+/+}$> WT ($n=8$) or *Pten*$^{Tg/+}$> WT ($n=9$) mice after 18 weeks of HFD feeding (**$P=0.0088$; two-tailed Student's *t*-test). **g**, Liver size and H&E staining of representative liver sections after 18 weeks on a HFD. **h**, Relative liver weight and steatosis scoring after 18 weeks of HFD feeding ($n=9$ *Pten*$^{+/+}$> WT, $n=8$ *Pten*$^{Tg/+}$> WT (liver weight), $n=7$ *Pten*$^{Tg/+}$> WT (steatosis); ***$P=0.0004$; two-tailed Student's *t*-test). **i**, Hepatic transcript levels of lipogenic genes of *Pten*$^{+/+}$> WT ($n=8$) or *Pten*$^{Tg/+}$> WT ($n=9$) mice, 18 weeks after HFD feeding (**$P=0.0037$, **$P=0.0074$ and *$P=0.0342$; two-tailed Student's *t*-test). **j**, *Pten* and pro-inflammatory cytokine expression of FACS-sorted F4/80$^+$CD11b$^+$CD11c$^+$ ATMs from *Pten*$^{+/+}$> WT or *Pten*$^{Tg/+}$> WT mice, 16 weeks after HFD feeding ($n=5$ per genotype; ****$P<0.0001$ and *$P=0.0301$; two-tailed Student's *t*-test). Data are the mean ± s.e.m. and representative of one (**b** and **d**–**j**) or two (**c**) independent experiments.

Further, tumour-necrosis factor (TNF)-α, interleukin (IL)-1β and IL-6 expression was similar between ATMs of *Pten*$^{\Delta myel}$ HFD-fed animals and controls, suggesting that the beneficial effects of increased myeloid PI3K activity on metabolic health in obesity were independent of ATM cytokine profiles (Fig. 2h).

Together, although insulin secretion and hepatic lipogenic transcription were not reciprocally regulated between the *Pten*$^{Tg/+}$ BMT and *Pten*$^{\Delta myel}$ conditional model, possibly due to PTEN overexpression in adaptive immune cells in the former approach, both HFD-fed genetic models clearly demonstrated a reciprocal regulation in hepatic lipotoxicity. This suggests potential roles for myeloid PI3K signalling in metabolic health, linked to ATM-mediated lipid scavenging within adipose tissue, a process governing ectopic lipid deposition[1,7,11].

Lipid-laden ATMs are characterized by a CD11c$^+$CD206$^+$ signature. Therefore, we next characterized ATMs in obesity according to their lipid load using BODIPY staining. Dysregulated adipose tissue homeostasis heightens lipid exposure of ATMs, inducing a CD11c-positive ATM population[10,24,25]. During ST-HFD, CD11c-expressing (FBC: F4/80$^+$CD11b$^+$CD11c$^+$) ATMs exhibited higher neutral lipids compared to CD11c-negative (FB: F4/80$^+$CD11b$^+$CD11c$^-$) ATMs (Fig. 3a and Extended Data Fig. 4a). CD206 is a marker for lipid-associated macrophages[7], and the CD11c$^+$CD206$^+$ signature in humans has been assigned to 'crown-like' structures, handling lipids arising from dead adipocytes[31]. In line with their higher intracellular lipid load after ST-HFD, FBC ATMs displayed enhanced CD206 surface expression (Fig. 3a). Prolonged HFD feeding produced identical results, with FBC ATMs exhibiting higher intracellular lipids and CD206 expression compared to FB macrophages (Fig. 3b). Importantly, compared to FB and FBC populations, FBC ATMs expressing CD206 (FBC206) were richest in intracellular neutral lipids (Fig. 3c) and, concordantly, displayed the largest cell size after prolonged HFD feeding (Extended Data Fig. 4d–f). Recent reports have identified triggering

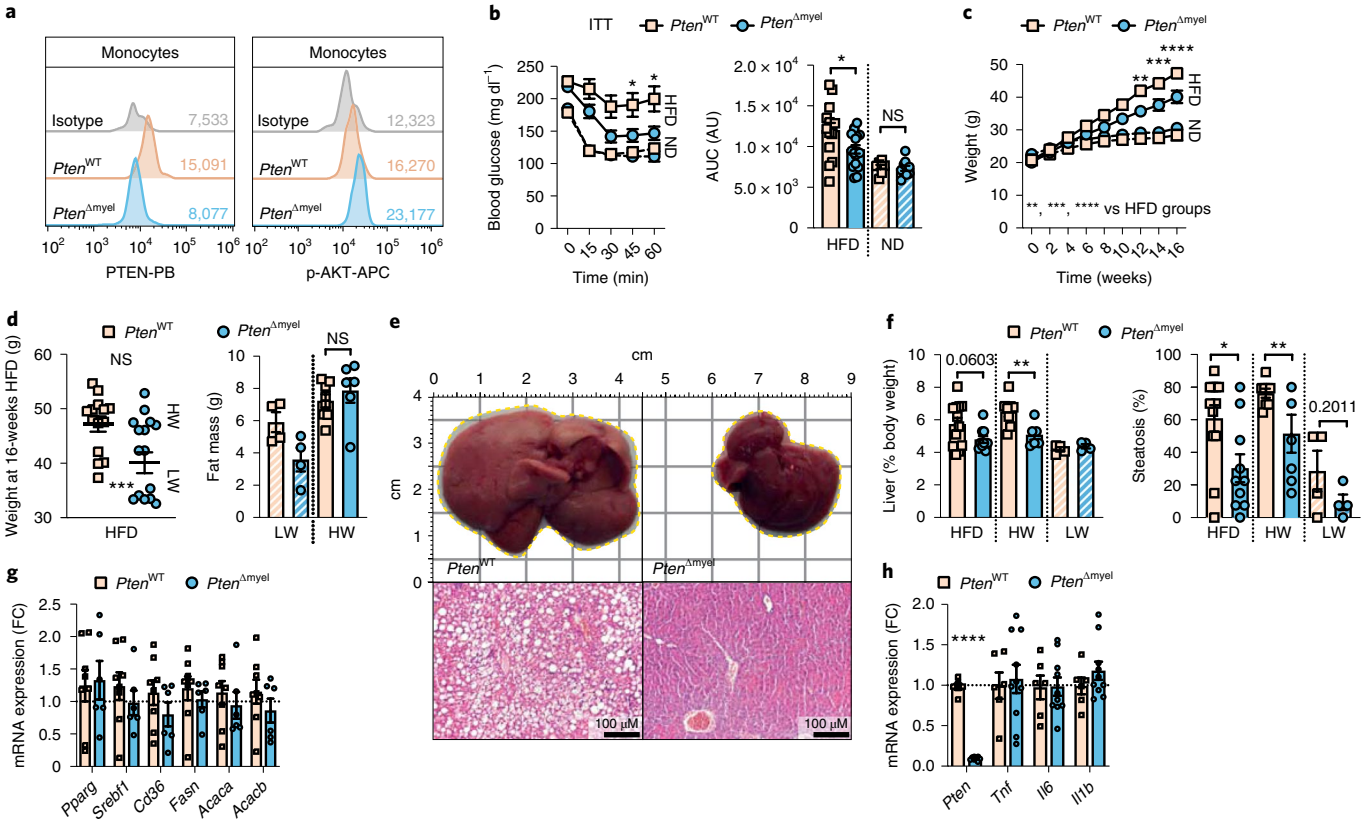

Fig. 2 | Sustained myeloid-cell-intrinsic PI3K activity via myeloid-specific PTEN deletion improves metabolic health in obesity. a, Histograms depicting PTEN and p-AKT expression in blood monocytes from *Pten*^{WT} or *Pten*$^{\Delta myel}$ animals. Cells were gated on CD45$^+$CD11b$^+$CD3$^-$B220$^-$Ly6G$^-$Ly6C$^+$. Isotype control samples depicted are identical to those in Fig. 1b. **b**, Insulin tolerance test (ITT) and AUC of *Pten*^{WT} ($n=8$ ND; $n=17$ HFD) or *Pten*$^{\Delta myel}$ ($n=10$ ND; $n=14$ HFD) mice after 16 weeks of feeding (*$P=0.0433$ and *$P=0.0175$; two-way ANOVA of HFD groups with Bonferroni's correction; *$P=0.0241$ for AUC; two-tailed Student's *t*-test). **c**,**d**, Weights of HFD mice shown in **b** stratified for LW and HW and corresponding end-point weights and fat mass ($n=8$ *Pten*^{WT} ND; $n=10$ *Pten*$^{\Delta myel}$ ND; $n=14$ *Pten*$^{\Delta myel}$ HFD; $n=17$ *Pten*^{WT} HFD; stratified: $n=4$ *Pten*^{WT} LW; $n=10$ *Pten*^{WT} HW; $n=8$ *Pten*$^{\Delta myel}$ LW; $n=9$ *Pten*$^{\Delta myel}$ HW; **$P=0.0016$, ***$P=0.0005$ and ****$P<0.0001$, two-way ANOVA of HFD groups with Bonferroni's correction; ***$P=0.0006$, one-way ANOVA of LW groups with Bonferroni's correction). **e**, Liver size and H&E staining of representative liver sections after 18 weeks on a HFD. **f**, Relative liver weight and steatosis scoring after 18 weeks' HFD feeding (n = 4 *Pten*^{WT} LW, n = 8 *Pten*^{WT} HW, $n=4$ *Pten*$^{\Delta myel}$ LW, $n=6$ *Pten*$^{\Delta myel}$ HW, **$P=0.0073$, *$P=0.0175$, **$P=0.0058$; two-tailed Student's *t*-test). **g**, Hepatic transcript levels of lipogenic genes of *Pten*^{WT} ($n=8$) or *Pten*$^{\Delta myel}$ ($n=6$) mice after 18 weeks of HFD feeding. **h**. *Pten* and pro-inflammatory cytokine expression of FACS-sorted F4/80$^+$CD11b$^+$CD11c$^+$ ATMs from *Pten*^{WT} ($n=6$) or *Pten*$^{\Delta myel}$ ($n=10$) mice after 16 weeks' HFD feeding (****$P<0.0001$; two-tailed Student's *t*-test). Data are the mean ± s.e.m. and representative of one (**a**, **g** and **h**) or pooled from two (**b**–**f**) independent experiments.

receptor expressed on myeloid cells 2 (TREM-2) and CD9 as markers for lipid-associated macrophages in obesity[6,7]. Notably, after ST-HFD, FBC206 ATMs expressed both markers (Extended Data Fig. 4g). In accordance with obesity-associated FBC ATMs exhibiting a lysosomal signature connected to lipid handling[10] (Extended Data Fig. 4h), FBC206 ATMs displayed the highest lysosomal numbers (Extended Data Fig. 4i).

To identify if lipid-rich FBC206 ATMs originated from resident ATMs or infiltrating monocytes and to examine which population buffered lipids, we utilized *Ccr2*$^{GFP/GFP}$ animals with defective CCR2-dependent monocyte influx and *Ccr2*$^{GFP/+}$ animals to track monocytes. When injected with CL316,243, weight-matched CCR2-sufficient and CCR2-deficient animals showed expected increases in serum non-esterified fatty acids (NEFAs) and decreases in glucose. There were no differences between genotypes, suggesting negligible influences of circulation-derived cells on lipid handling after acute lipolysis (Fig. 3d). We next compared GFP$^+$ circulation-derived versus GFP$^-$ resident macrophages in adipose tissue after lipolysis. While the FBC population mainly comprised GFP$^+$ infiltrating cells, the majority of FBC206 ATMs were GFP$^-$ (Fig. 3e,f).

To exclude insufficient time for infiltrating monocytes to give rise to FBC206 ATMs in acute lipolysis, we compared GFP$^+$ circulation-derived versus GFP$^-$ resident macrophages in adipose tissue after a ST-HFD. Demonstrating comparable effects, approximately 40% of FBC206 and 80% of FBC ATMs were GFP$^+$ (Extended Data Fig. 4j). Notably, the GFP$^-$ATMs after acute lipolysis were highest in lysosomes, suggesting resident macrophages might be 'imprinted' to handle and metabolize adipocyte-derived lipid spillover (Fig. 3g). In agreement with the results of HFD feeding, after acute lipolysis, FBC206 ATMs displayed substantially increased lipid content compared to FBC ATMs (Fig. 3h). Thus, in both acute lipolysis and a ST-HFD, although a portion of FBC206 ATMs originates from circulating monocytes, over half are resident and more lipid laden than circulation-derived FBC ATMs.

To characterize the lipid-buffering ability of FBC206 ATMs compared to other cells types including blood monocytes and liver myeloid cells in obesity, we next injected the fluorescent fatty acid C16 BODIPY into HFD-fed animals, assessing how much each cell type acquired. Compared to hepatic myeloid cells, ATMs and blood monocytes were substantially more C16-BODIPY positive (Fig. 3i,j

and Extended Data Fig. 4b,c). Importantly, compared to FBC ATMs, FBC206 ATMs exhibited more C16-BODIPY mean fluorescence intensity (MFI; Fig. 3k). To ultimately confirm that FBC206 ATMs are most adept at lipid storage in obesity and to identify potential lipid preferences, we conducted targeted lipidomics of ATMs after HFD feeding. Strikingly, compared to FBC, FBC206 ATMs displayed an increased abundance of almost all lipid species examined (Fig. 3l). Thus, in the context of a lipid-rich environment, resident FBC206 ATMs most efficiently buffer lipids.

PI3K influences FBC206 ATMs generation after metabolic stress. We next examined the possible cross-talk among metabolically stressed adipose signals, FBC206 ATMs and PI3K. We added ACM from HFD-fed animals to naïve macrophages, and the findings were similar to our in vivo observations, resulting in the generation of FBC206-expressing cells (Fig. 4a) associated with increased lipid content (Fig. 4a). In obesity, ATMs encounter excessive amounts of metabolic stimuli, including glucose, insulin or lipids, triggering a metabolically activated phenotype, coined MMe activation[9,11]. We next defined which ACM components induced FBC206 macrophages. While glucose, insulin, cytokines and adipokines typically found in ACM had no effect, ACM robustly and reproducibly led to their induction (Extended Data Fig. 5a,b). Further, FBC206-expressing cells were not generated from naïve macrophages challenged with cholesterol, unsaturated oleic acid or saturated palmitic acid (Extended Data Fig. 5c), or by the simultaneous addition of glucose, insulin and palmitate (MMe activation)[9,11] (Extended Data Fig. 5d). This suggested that either unknown ACM components, synergy among cytokines and lipids or complex fatty acid mixtures might act as signals. Indeed, free fatty acid supplementation (FAS) enhanced both FBC206 relative to FBC generation and lipid content (Fig. 4b,c).

Although palmitate did not lead to FBC206 ATM generation (Extended Data Fig. 5c), long-chain fatty acids including palmitate reportedly alter the macrophage lipidome and cellular metabolism via Toll like receptor 4 (TLR4)[32]. We therefore examined if ACM-mediated FBC206 expression occurred via TLR4. Treatment of macrophages with the TLR4 antagonist resatorvid (TAK-242) exerted no influences on ACM-induced FBC206 expression (Extended Data Fig. 5e). Together, in macrophages, complex mixtures of ACM-derived fatty acids induce FBC206 expression through a yet-unidentified upstream mechanism.

Focusing on downstream signalling, we next examined whether ACM-mediated FBC206 generation depends on macrophage-intrinsic PI3K activity. PI3K inhibition with the US Food and Drug Administration–approved PI3Kγ/δ inhibitor duvelisib[33] abrogated macrophage ACM-induced FBC206 generation and lipid loading (Fig. 4d). As confirmation of the involvement of PI3K, *Pten*-deficient macrophages displayed enhanced FBC206 generation after ACM (Fig. 4e). We next wondered if increases in this ATM population are causally implicated in metabolic health improvements of obese $Pten^{\Delta myel}$ animals (Fig. 2). Strikingly, $Pten^{\Delta myel}$ mice displayed a marked shift towards more FBC206 ATMs than FBC ATMs 16 weeks after HFD feeding compared to controls (Fig. 4f). Increased FBC206 ATMs were also observed in $Pten^{\Delta myel}$ animals after a ST-HFD (Fig. 4g), together with expected PTEN deletion and augmented PI3K signalling within the ATM pool (Fig. 4h). To confirm equal PTEN deletion efficiency within the ATM subsets, we isolated ATMs from $Pten^{\Delta myel}R26^{tdTomato}$ reporter mice[34] after a ST-HFD and analysed their tomato expression. Compared with ATMs of a Cre^{-} control, 100% of ATM subsets from $Pten^{\Delta myel}R26^{tdTomato}$ animals were positive for tomato, demonstrating equivalent Cre-targeting (Extended Data Fig. 6a). Similarly, PTEN was equally deleted in all ATM populations versus the Cre^{-} control (Extended Data Fig. 6a). Together, these data indicate that enhanced myeloid-cell-intrinsic PI3K activity influences FBC206 ATM generation in response to signals from metabolically stressed adipose tissue.

MARCO is a marker of lipid-laden FBC206 ATMs that is regulated by PI3K. We next investigated whether ATMs buffer lipids via scavenger receptors that are important for lipid uptake[35,36]. We mined a publicly available dataset, comparing FB and lipid-associated FBC populations in leptin-deficiency-induced murine obesity. We found a significant induction in macrophage receptor with collagenous structure (MARCO) expression in FBC versus FB ATMs, which was notably higher than the classic lipid-uptake scavenger receptor CD36 (ref. [36]; Fig. 5a). MARCO surface levels of ATM subsets of obese mice confirmed this, demonstrating that increased MARCO levels on FBC versus FB ATMs were surpassed by the previously established lipid-rich FBC206 ATMs (Fig. 5b). Elevated MARCO expression on FBC206 versus FBC ATMs was unique in obesity and not observed in ND-fed animals (Fig. 5c). These data suggested a link between myeloid MARCO induction with obesity-induced perturbations in adipose tissue homeostasis.

We could reproduce the high MARCO surface expression on FBC206 ATMs in the context of a ST-HFD and CL316,243 (Extended Data Fig. 6b,c). Although disruption of adipose tissue homeostasis after lipolysis led to macrophage p-AKT loss in vivo (Extended Data Fig. 1), in comparison to FBC macrophages, the lipid-handling FBC206 ATMs retained a significantly higher p-AKT signature following HFD feeding and acute lipolysis (Fig. 5d and Extended Data Fig. 6d). Differences in p-AKT in between ATM populations were absent after ND feeding (Fig. 5e), suggesting FBC206 ATMs conserved their cell-intrinsic PI3K–AKT signalling and that MARCO induction coincides with preserved PI3K activity.

Fig. 3 | Resident FBC206 ATMs are induced by lipids and dysregulation in adipose tissue homeostasis and most efficiently buffer lipids in obesity. **a**, MFI of BODIPY and CD206 in macrophages after ST-HFD. Cells were pregated on viable $CD45^{+}CD11b^{+}F4/80^{+}$ and are displayed as CD11c-negative (FB) or CD11c-positive (FBC) populations after a ST-HFD ($n=5$ animals; $^{*}P=0.0455$ and $^{****}P<0.0001$; two-tailed Student's *t*-test). **b**, MFI of BODIPY and CD206 in macrophages after 16 weeks' HFD feeding ($n=5$ animals; $^{****}P<0.0001$ and $^{***}P=0.0001$; two-tailed Student's *t*-test). **c**, BODIPY MFI of the CD11c and CD206 double-positive ATM population (FBC206) after 16 weeks' HFD feeding ($n=8$ animals; $^{**}P=0.0086$ and $^{**}P=0.0011$; one-way ANOVA with Bonferroni's correction). **d**, Plasma NEFA and glucose levels following CL316,243-induced lipolysis in $Ccr2^{+/+}$ and $Ccr2^{GFP/+}$ mice and corresponding weights ($n=6$ animals per genotype). **e**, After acute lipolysis, infiltrating and resident eWAT-associated macrophage populations were analysed for their FBC206 signature in $Ccr2^{GFP/+}$ animals, and eWAT was collected from mice injected twice with 1 mg kg^{-1} CL316,243 at 18 h and 14 h before harvest. SVF, stromal vascular fraction. **f**,**g**, The percentages of $GFP^{+}FBC^{-}$ versus GFP^{+} FBC206 ATMs and GFP^{-} FBC^{-} versus GFP^{-} FBC206 ATMs (**f**) and their LysoTracker MFI in eWAT after lipolysis (**g**) of $Ccr2^{GFP/+}$ reporter mice. Cells were pregated on $CD45^{+}CD11b^{+}F4/80^{+}$ ($n=6$ animals; $^{****}P<0.0001$ and $^{***}P=0.0005$, two-tailed Student's *t*-test; $^{****}P<0.0001$, two-way ANOVA with Bonferroni's correction). **h**, BODIPY MFI of the FBC versus FBC206 ATM populations (FBC206) after CL316,243 ($n=5$ animals; $^{**}P=0.0032$; two-tailed Student's *t*-test). **i**, The percentage of C16-BODIPY-positive ATMs, monocytes and hepatic myeloid cells (MOs) from 16-week HFD-fed animals (gated as in Extended data Fig. 4a–c) 1 h after injection ($n=3$ animals; $^{***}P=0.0004$ and $^{***}P=0.0001$; one-way ANOVA with Bonferroni's correction). **j**, Flow cytometry plots are representative of data shown in **i**. **k**, C16-BODIPY MFI in FBC and FBC206 ATMs 1 h after injection ($n=4$ animals; $^{**}P=0.0080$; two-tailed Student's *t*-test). **l**, Lipidomics of FACS-sorted FBC and FBC206 ATMs after a ST-HFD ($n=4$ animals). Data are the mean ± s.e.m. and representative of one (**h**–**k**), two (**a**, **d**, **f** and **g**) or four (**b** and **c**) independent experiments. AU, arbitrary units.

MARCO expression is reportedly regulated by the oxidative-stress-sensitive transcription factor nuclear factor erythroid 2-related factor 2 (NRF2), described to be triggered by the PI3K–AKT pathway[37]. Confirming this, we observed significantly decreased basal MARCO surface expression on *Nrf2*$^{-/-}$ primary peritoneal macrophages in vitro (Fig. 5f). To strengthen the evidence that MARCO expression depends on PI3K activity via NRF2, we again used myeloid *Pten* deficiency to model PI3K overactivation. *Pten*$^{\Delta myel}$ macrophages displayed increased basal MARCO surface expression and strong tendencies towards elevated NRF2 DNA-binding activity (Fig. 5g,h). Using the opposite genetic approach, we confirmed decreased MARCO levels in *Pten*$^{Tg/+}$ macrophages (Fig. 5i). Pharmacological PI3K inhibition with wortmannin decreased MARCO surface levels in WT cells, reversing the genotype-specific MARCO increases of *Pten*$^{\Delta myel}$ macrophages (Fig. 5j). To demonstrate that MARCO expression relied on NRF2 activity downstream of elevated PI3K, we inhibited NRF2 activity via brusatol treatment[38] in *Pten*$^{\Delta myel}$ macrophages and observed substantially reduced MARCO expression (Fig. 5k). These data imply that, in opposition to the roles for PTEN independent of PI3K, elevated PI3K catalytic activity in *Pten*$^{\Delta myel}$ macrophages regulates MARCO expression via NRF2 activation. Supporting this,

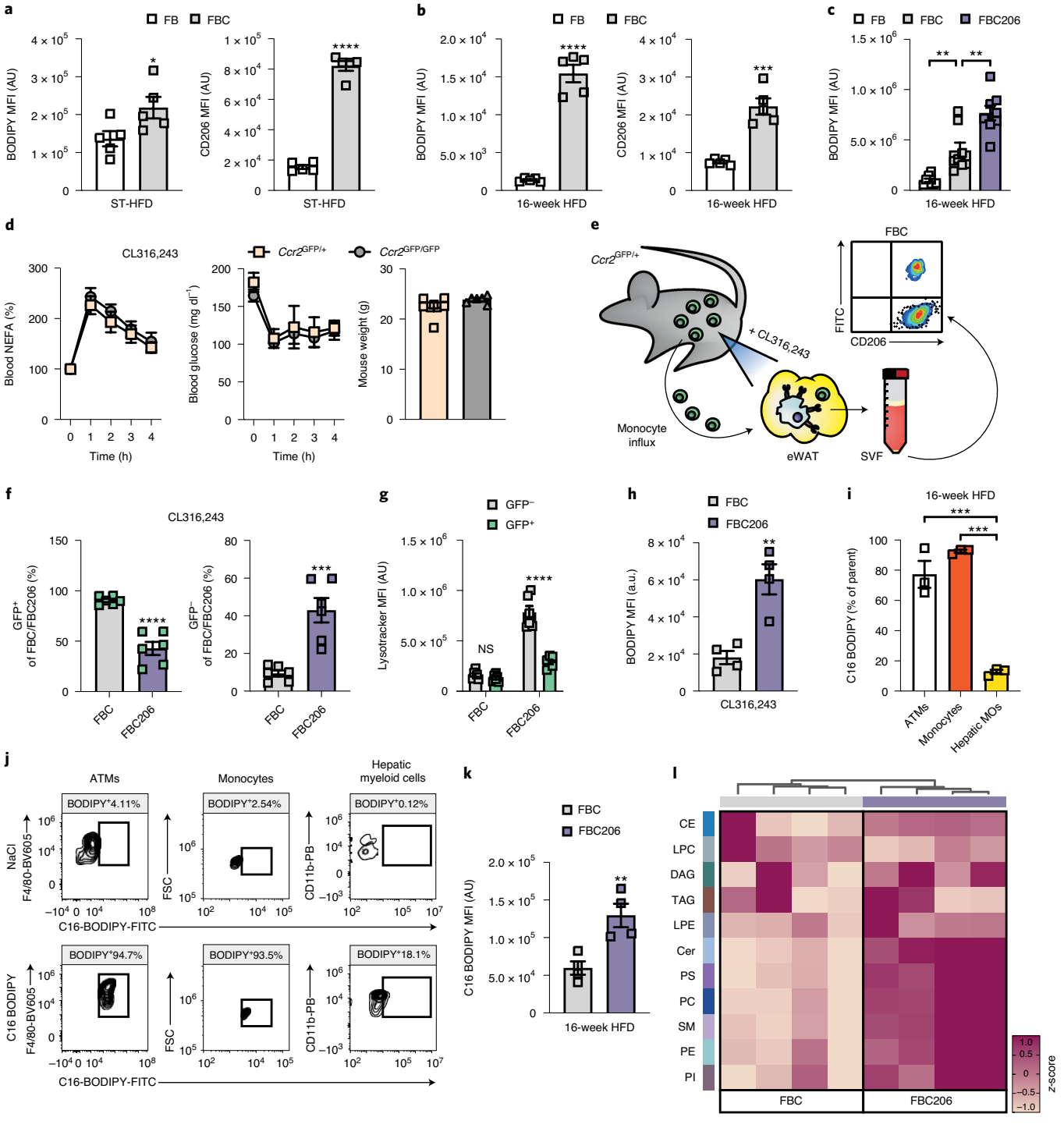

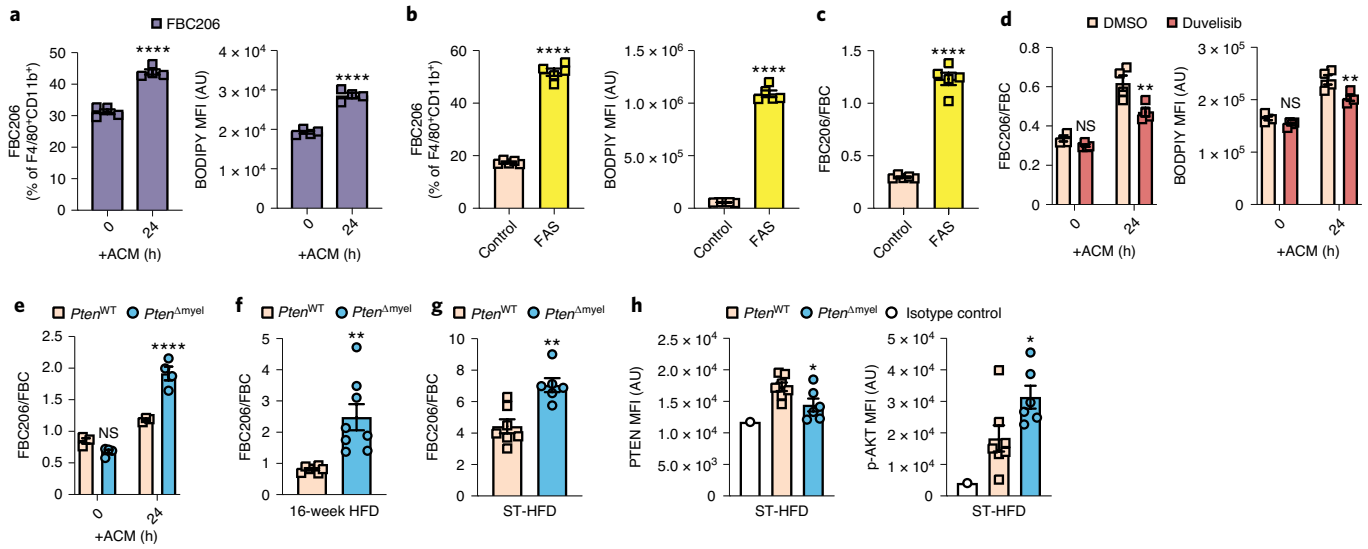

Fig. 4 | Myeloid-cell-intrinsic PI3K signalling is critical for FBC206 ATM generation. a, The percentage of FBC206 macrophages and their BODIPY MFI after 24-h ACM treatment of naïve macrophages ($n=4$ samples; $^{****}P<0.0001$; two-tailed Student's t-test). **b**, The percentage of FBC206 macrophages and BODIPY MFI after 24-h FAS of naïve macrophages ($n=5$ samples; $^{****}P<0.0001$; two-tailed Student's t-test). **c**, FBC206/FBC ratio of data in **b** ($^{****}P<0.0001$; two-tailed Student's t-test). **d**, FBC206/FBC ratio and BODIPY MFI of naïve macrophages treated with duvelisib and subsequently challenged with ACM for 24 h ($n=4$ samples; $^{**}P=0.0015$ and $^{**}P=0.0019$; two-way ANOVA with Bonferroni's correction); DMSO, dimethylsulfoxide. **e**, FBC206/FBC ratio of *Pten*^{WT} ($n=3$ samples) and *Pten*$^{\Delta myel}$ ($n=4$ samples) macrophages challenged with ACM for 24 h ($^{****}P<0.0001$; two-way ANOVA with Bonferroni's correction). **f**, FBC206/FBC ratio in eWAT of *Pten*^{WT} ($n=7$) or *Pten*$^{\Delta myel}$ ($n=8$) animals 16 weeks after HFD. Cells were gated on viable CD45$^+$CD11b$^+$F4/80$^+$CD11c$^+$CD206$^{+/-}$ ($^{**}P=0.0026$; two-tailed Student's t-test). **g**,**h**, FBC206/FBC ratio (**g**) and corresponding PTEN deletion efficiency and p-AKT in eWAT of *Pten*^{WT} ($n=7$) or *Pten*$^{\Delta myel}$ ($n=6$) animals after ST-HFD feeding (**h**). Cells were gated on viable CD45$^+$CD11b$^+$F4/80$^+$CD11c$^+$CD206$^{+/-}$ (**g**) and CD45$^+$CD11b$^+$F4/80$^+$ (**h**) ($^{**}P=0.0016$, $^{*}P=0.0394$ and $^{*}P=0.0342$; two-tailed Student's t-test). Data are the mean ± s.e.m. and representative of one (**g** and **h**), two (**d**–**f**) or three (**a**–**c**) independent experiments.

macrophages genetically deficient in AKT1/2, which are downstream of PI3K, displayed decreased MARCO and its levels were also decreased after PI3Kγ/δ inhibition with duvelisib[33] (Fig. 5l,m).

To ultimately demonstrate that PI3K catalytic activity regulated MARCO expression, we utilized catalytically inactive *Pi3kγ*$^{KD/KD}$ macrophages[39] and observed decreased MARCO levels (Fig. 5n). In agreement with data indicating that PI3K activity influences FBC206 ATM generation in obesity and that MARCO expression depends on PI3K catalytic activity, MARCO levels were increased in HFD-fed *Pten*$^{\Delta myel}$ animals compared to controls (Fig. 5o). Together, these data indicate a critical role for PI3K–AKT–NRF2 signalling in regulating MARCO expression and demonstrate that lipid-buffering FBC206 ATMs are characterized by enhanced MARCO surface expression.

MARCO is required for efficient lipid buffering. We next determined whether MARCO influences the lipid uptake capability of FBC206 ATMs. MARCO deficiency within macrophages was associated with decreased lipid content after in vitro ACM and fatty acid challenge, suggesting macrophage MARCO expression is associated with buffering lipids (Fig. 6a,b). By subjecting *Marco*$^{-/-}$ and control animals to acute lipolysis, we observed higher blood NEFAs and lower blood glucose in *Marco*$^{-/-}$ mice compared to controls (Fig. 6c), independent of weight and fat depot mass (Extended Data Fig. 7a,b). Although adipocytes did not express MARCO (Extended Data Fig. 7c), to exclude contributions of adipose-specific differences, we subjected isolated weight-matched eWAT from both genotypes to isoproterenol-induced lipolysis. We did not observe any differences, suggesting that increased NEFAs of *Marco*$^{-/-}$ animals after β3-adrenoceptor agonism were dependent on impaired macrophage lipid uptake (Extended Data Fig. 7d).

We next examined if MARCO deficiency aggravated systemic insulin resistance. While no differences were observed during ND, long-term HFD-fed *Marco*$^{-/-}$ animals were less insulin sensitive (Fig. 6d), independently of weight gain and adiposity (Extended Data Fig. 7e,f). Further, HFD-fed *Marco*$^{-/-}$ mice displayed impaired glucose tolerance compared to weight-matched controls (Fig. 6e and Extended Data Fig. 7g). After HFD feeding, we noted equal macrophage numbers in eWAT of *Marco*$^{-/-}$ animals compared to controls, but significantly less lipid-buffering FBC206 ATMs (Fig. 6f). Before HFD feeding, *Marco*$^{-/-}$ animals did not exhibit baseline differences in ATM content or in FBC206/FBC ATM ratios (Extended Data Fig. 7h). Underscoring the importance of MARCO for myeloid lipid uptake in obesity, MARCO-deficient FBC206 ATMs contained significantly fewer neutral lipids (Fig. 6g). These data and those indicating reduced lipid uptake in *Marco*$^{-/-}$ macrophages (Fig. 6a) suggest that MARCO deficiency might lead to attenuated ACM-mediated FBC206 induction. Indeed, this was the case, suggesting that MARCO-dependent lipid uptake sustains FBC206 ATM generation (Fig. 6h). We therefore identified MARCO as a protective factor important for lipid buffering and maintenance of metabolic health.

The PI3K pathway boosts macrophage lipid metabolism. As our data demonstrated that increased myeloid PI3K signalling in obesity results in more lipid-handling FBC206 ATMs exhibiting high MARCO surface expression (Fig. 4f and Fig. 5o), we wondered if PI3K drives myeloid-cell-intrinsic lipid uptake and metabolism. Supporting this, PTEN-deficient macrophages exhibited enhanced fatty acid and acetylated low-density lipoprotein (LDL) uptake in vitro, most likely partially via their increased MARCO levels (Figs. 5o and 7a,b and Extended Data Fig. 8a). Intriguingly, at baseline, we observed augmented intracellular neutral lipids within

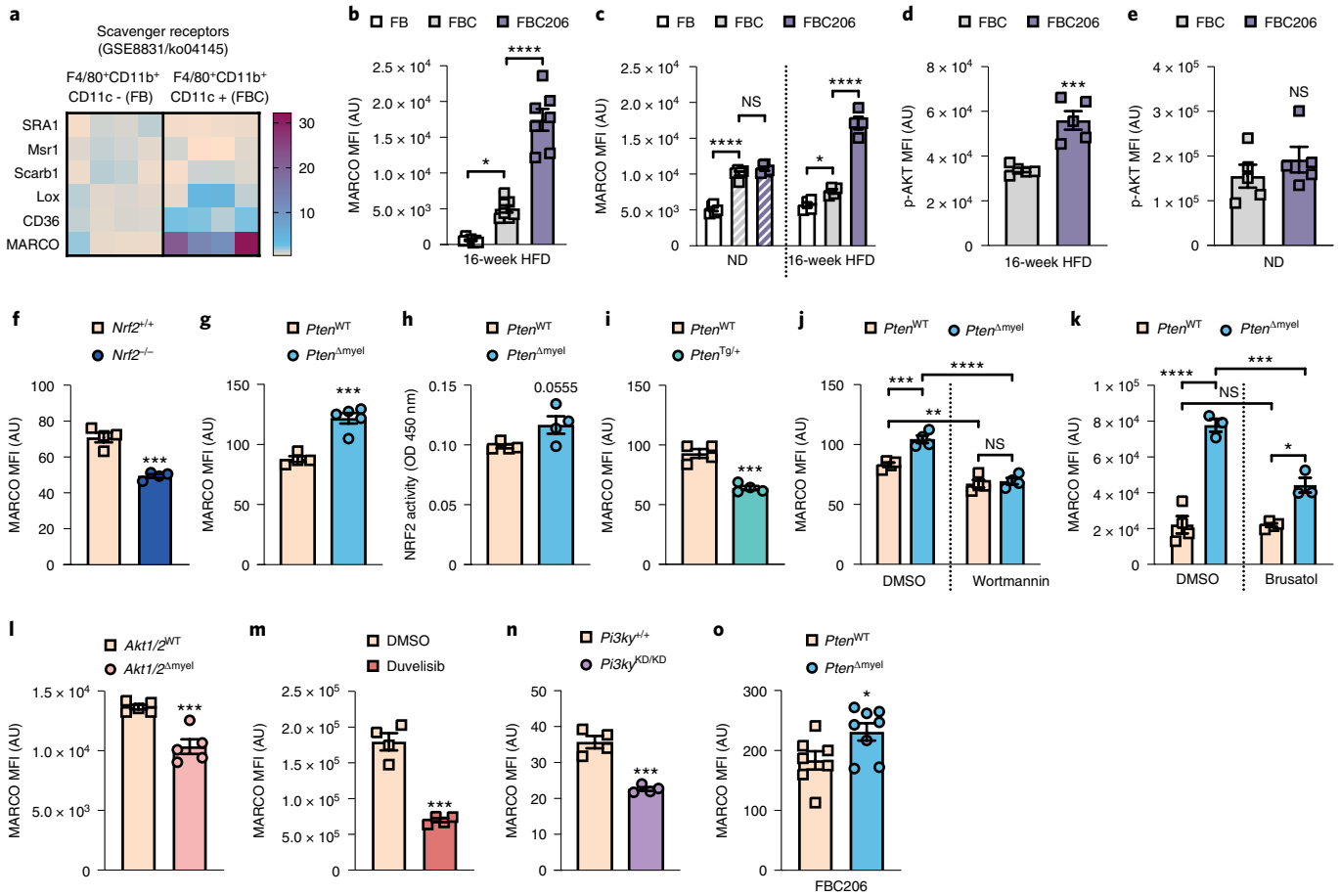

Fig. 5 | MARCO is a marker for lipid-laden FBC206 ATMs in obesity and is regulated by the PI3K–Nrf2 pathway. a, Public microarray scavenger receptor expression data of FB macrophages from obese mice versus FBC ATMs depicted as the fold change (FC) relative to FB cells. **b**, MARCO MFI in macrophages after a HFD ($n=7$ animals; $^{*}P=0.0109$, $^{****}P<0.0001$; one-way ANOVA with Bonferroni's correction). **c**, MARCO MFI in macrophages after HFD ($n=4$) versus ND ($n=5$; $^{****}P<0.0001$, $^{*}P=0.0157$ and $^{****}P<0.0001$; two-way ANOVA with Bonferroni's correction). **d**, p-AKT MFI of FBC and FBC206 ATMs after a HFD ($n=5$ animals; $^{***}P=0.0008$; two-tailed Student's *t*-test). **e**, p-AKT MFI of FBC and FBC206 ATMs of ND-fed mice ($n=5$ animals). **f**, MARCO MFI of *Nrf2*$^{+/+}$ and *Nrf2*$^{-/-}$ macrophages ($n=4$ samples; $^{***}P=0.0003$; two-tailed Student's *t*-test). **g**, MARCO MFI of *Pten*^{WT} ($n=4$ samples) and *Pten*$^{\Delta myel}$ ($n=5$ samples) macrophages ($^{***}P=0.0004$; two-tailed Student's *t*-test). **h**, NRF2 DNA-binding activity in *Pten*^{WT} and *Pten*$^{\Delta myel}$ macrophages ($n=4$ samples; two-tailed Student's *t*-test). **i**, MARCO MFI of *Pten*$^{+/+}$ and *Pten*$^{Tg/+}$ macrophages ($n=4$ samples; $^{***}P=0.0004$; two-tailed Student's *t*-test). **j**, MARCO MFI of wortmannin-treated *Pten*^{WT} and *Pten*$^{\Delta myel}$ macrophages ($n=4$ samples; $^{***}P=0.0008$, $^{**}P=0.0082$, $^{****}P<0.0001$; one-way ANOVA with Bonferroni's correction). **k**, MARCO MFI of brusatol-treated *Pten*^{WT} ($n=4$ samples) and *Pten*$^{\Delta myel}$ ($n=3$ samples) macrophages ($^{****}P<0.0001$, $^{***}P=0.0007$, $^{*}P=0.0103$; one-way ANOVA with Bonferroni's correction). **l**, MARCO MFI of *Akt1/2*^{WT} and *Akt1/2*$^{\Delta myel}$ macrophages ($n=5$ samples; $^{***}P=0.0009$; two-tailed Student's *t*-test). **m**, MARCO MFI of duvelisib-treated macrophages ($n=4$ samples; $^{***}P=0.0001$; two-tailed Student's *t*-test). **n**, MARCO MFI of *Pi3kγ*$^{+/+}$ and *Pi3kγ*$^{KD/KD}$ macrophages ($n=4$ samples; $^{***}P=0.0003$; two-tailed Student's *t*-test). **o**, MARCO MFI of FBC206 ATMs of *Pten*^{WT} ($n=7$ animals) or *Pten*$^{\Delta myel}$ ($n=8$ animals) 16 weeks after a HFD ($^{*}P=0.0411$; two-tailed Student's *t*-test). Data are the mean ± s.e.m. and representative of one (**c**, **h** and **o**), two (**d**–**f** and **i**–**n**) or three (**b**, **l** and **g**) independent experiments.

PTEN-deficient macrophages (Fig. 7c). To gain further insights, we performed lipidomics analysis. We did not identify increases in distinct lipids, but rather observed a globally skewed lipid profile indicating increased lipid abundance within macrophages featuring constitutive active PI3K signalling (Fig. 7d). In accordance with the role of PI3K in the formation of FBC206 ATMs (Fig. 4d–g), lipid profiles of naïve PTEN-deficient macrophages markedly resembled FBC206 ATMs from HFD-fed animals (Fig. 7d and Fig. 3l).

In alternatively activated macrophages, cell-intrinsic lipids are taken up via CD36, degraded in the lysosome and fuelled into fatty acid oxidation to generate energy[40]. Concordantly with elevated lipid presence, we observed drastic increases in baseline oxidative phosphorylation (OXPHOS), independent of mitochondrial numbers in PTEN-deficient cells compared to controls (Fig. 7e and Extended Data Fig. 8b,c). Although there were significant increases in PGC-1α (*Ppargc1a*) and *Ppar-γ* baseline transcription in PTEN-deficient macrophages, there were no genotype-specific differences in other mitochondrial biogenesis or fatty acid metabolism/oxidation genes tested (Extended Data Fig. 8d). PTEN-deficient macrophages also exhibited an enhanced basal extracellular acidification rate (ECAR), a proxy for cellular glycolytic activity (Extended Data Fig. 8e). Although cellular metabolism of *Pten*$^{Tg/+}$ macrophages showed decreased OXPHOS, the ECAR was unchanged (Fig. 7f and Extended Data Fig. 8f). Obesity-related changes in the adipose tissue microenvironment reportedly shape ATM metabolism, driving glycolysis and OXPHOS[15]. This, along with our data, suggests that enhanced PI3K signalling could prepare macrophages to meet metabolic requirements for efficient catabolism of excess nutrients, especially lipids, typically encountered during obesity.

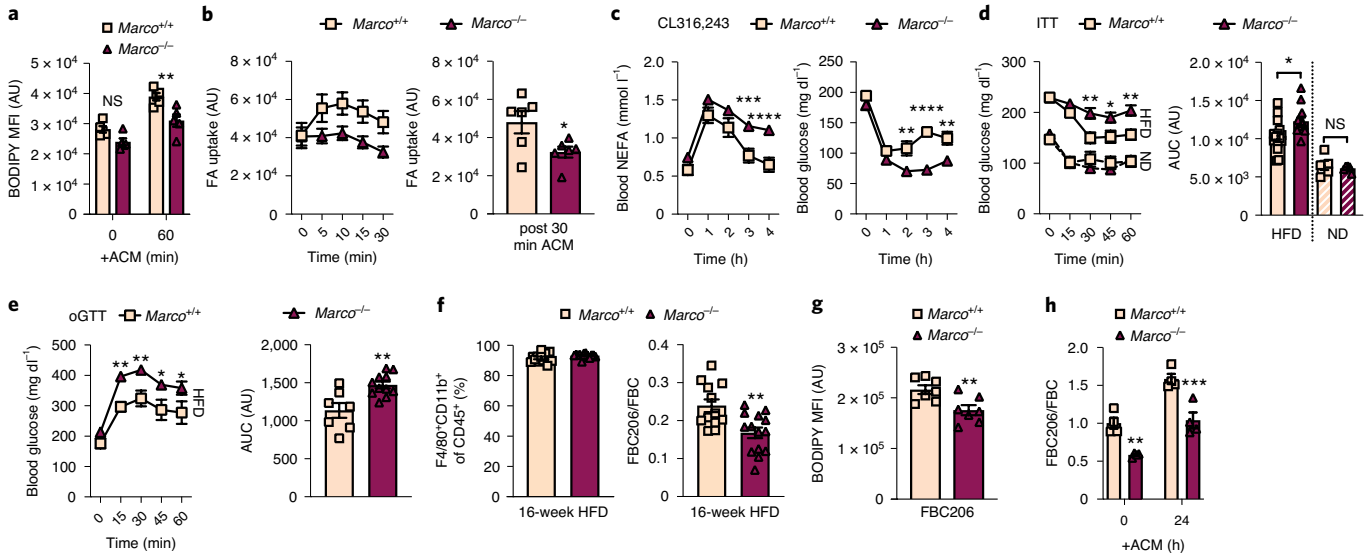

Fig. 6 | The scavenger receptor MARCO mediates lipid uptake. a, BODIPY MFI of *Marco*$^{+/+}$ and *Marco*$^{-/-}$ macrophages after treatment with ACM ($n=5$ samples; $^{**}P=0.0022$; two-way ANOVA with Bonferroni's correction). **b**, Fatty acid (FA) uptake in *Marco*$^{+/+}$ and *Marco*$^{-/-}$ macrophages ($n=6$ samples; $^{*}P=0.0364$; two-tailed Student's *t*-test). **c**, Plasma NEFA and glucose levels after CL316,243-induced lipolysis in *Marco*$^{+/+}$ ($n=5$) and *Marco*$^{-/-}$ ($n=7$) mice ($^{***}P=0.0010$ and $^{****}P<0.0001$; $^{**}P=0.0027$, $^{****}P<0.0001$ and $^{**}P=0.0031$; two-way ANOVA with Bonferroni's correction). **d**, ITT and AUC of *Marco*$^{+/+}$ ($n=5$ ND and $n=16$ HFD) and *Marco*$^{-/-}$ ($n=6$ ND and $n=14$ HFD) animals 16 weeks after HFD feeding ($^{**}P=0.004$, $^{*}P=0.0382$, $^{**}P=0.0043$; two-way ANOVA with Bonferroni's correction; $^{*}P$ for AUC = 0.0103; two-tailed Student's *t*-test). **e**, oGTT and AUC of *Marco*$^{+/+}$ ($n=7$) and *Marco*$^{-/-}$ ($n=11$) mice, 16 weeks after HFD feeding ($^{**}P=0.0036$, $^{**}P=0.0071$, $^{*}P=0.0234$ and $^{*}P=0.0286$; two-way ANOVA with Bonferroni's correction; $^{**}P$ for AUC = 0.0027; two-tailed Student's *t*-test). **f**, Macrophage infiltration and FBC206/FBC ratios of *Marco*$^{+/+}$ ($n=12$) and *Marco*$^{-/-}$ ($n=14$) mice after 16 weeks on a HFD. Cells were gated on viable CD45^{+}CD11b^{+}F4/80^{+}CD11c$^{+/-}$CD206$^{+/-}$ ($^{**}P=0.0030$; two-tailed Student's *t*-test). **g**, BODIPY MFI of MARCO-deficient FBC206 macrophages after 16 weeks on a HFD. Cells were gated on viable CD45^{+}CD11b^{+}F4/80^{+}CD11c^{+}CD206^{+} (FBC206) ($n=7$ animals per genotype; $^{**}P=0.0093$; two-tailed Student's *t*-test). **h**, FBC206/FBC ratio of *Marco*$^{+/+}$ and *Marco*$^{-/-}$ macrophages challenged with ACM for 24 h ($n=4$ samples; $^{**}P=0.0028$ and $^{***}P=0.0003$; two-way ANOVA with Bonferroni's correction). Data are the mean ± s.e.m. and representative of one (**e** and **g**), two (**a**–**c** and **h**) or are pooled from two (**f**) or four (**d**) independent experiments.

To further demonstrate that the increases in OXPHOS relied on fatty acid oxidation, we performed experiments using the Cpt1α/fatty acid oxidation inhibitor etomoxir[40]. Suggesting enhanced OXPHOS of *Pten*$^{\Delta myel}$ macrophages solely depended on fatty acid oxidation and lipid degradation, etomoxir lowered the spare respiratory capacity of PTEN-deficient macrophages to WT levels, while OXPHOS of *Pten*$^{Tg/+}$ macrophages was not further decreased (Fig. 7g,h and Extended Data Fig. 8g,h). In line with studies using adipose tissue co-cultures[15], lipid-rich ACM derived from HFD-fed animals induced macrophage OXPHOS (Fig. 7i). Supporting the hypothesis that myeloid PI3K-dependent macrophage lipid handling was linked to surface MARCO levels, *Marco*$^{-/-}$ macrophages were unable to induce OXPHOS after ACM (Fig. 7i), independent of baseline differences in representative gene expression of mitochondrial respiratory complexes (Extended Data Fig. 8i). These data show that PI3K crucially modulates intracellular metabolism and drives fatty acid oxidation and identify that MARCO-dependent lipid uptake fuels intracellular metabolism.

PI3K-instigated lipid uptake depends on MARCO expression. To tease apart MARCO-dependent effects on macrophage metabolism and lipid handling from PI3K-instigated ones, we crossed *Pten*$^{\Delta myel}$ with *Marco*$^{-/-}$ mice, generating *Pten*$^{\Delta myel}$*Marco*$^{-/-}$ double-deficient animals. Remarkably, the lipid content of *Pten*$^{\Delta myel}$*Marco*$^{-/-}$ macrophages was nearly identical to that of WT animals after ACM (Fig. 8a). This indicates that elevated PI3K-instigated MARCO expression (Fig. 5) largely mediated the increased lipid uptake of PTEN-deficient macrophages, observations corroborated using fatty acid uptake assays (Fig. 8b).

ATMs of obese mice express genes involved in fatty acid oxidation and lipolysis[15]; however, the metabolic fate of scavenged lipids and whether they are consumed, stored or recycled is ill-defined. We show that PTEN deficiency results in baseline increases in myeloid lipid uptake and intracellular lipid composition (Fig. 7a–d and Fig. 8a,b). To determine if these changes were dependent on *Pten* or *Marco* expression and to uncover lipid species specificity, we next performed lipidomics of ACM-treated *Pten*^{WT}, *Pten*$^{\Delta myel}$ and *Pten*$^{\Delta myel}$*Marco*$^{-/-}$ macrophages. Compared to the results in unstimulated *Pten*^{WT} controls, ACM stimulation resulted in robust intracellular increases in lipid species, including phosphatidylcholines (PCs), phosphatidylethanolamines (PEs), sphingomyelins (SMs) or diacylglycerides (DAGs) in *Pten*^{WT} macrophages (Fig. 8c; yellow ribbon). Suggestive of enhanced lipid consumption rather than storage, *Pten*$^{\Delta myel}$ macrophages displayed specific high enrichments in PCs, PEs and phosphatidylserines (PSs), while other species such as triacylglycerols (TAGs), DAGs and phosphatidylinositols (PIs) were decreased (Fig. 8c; blue ribbon). Double deficiency of both *Pten* and *Marco* lowered PTEN-dependent ACM-induced PC, PE and PS accumulation indicating that these lipid increases were largely MARCO dependent. The double knockout additionally decreased SM and DAG abundance and exhibited specific increases in lysophosphatidylcholine (LPC) and lysophosphatidylethanolamine (LPE), indicating MARCO-specific effects independent of PTEN deficiency (Fig. 8c; red ribbon). Lipidomic analysis thereby confirmed that enhanced lipid buffering mediated by PTEN-deficient macrophages heavily relied on their increased MARCO levels.

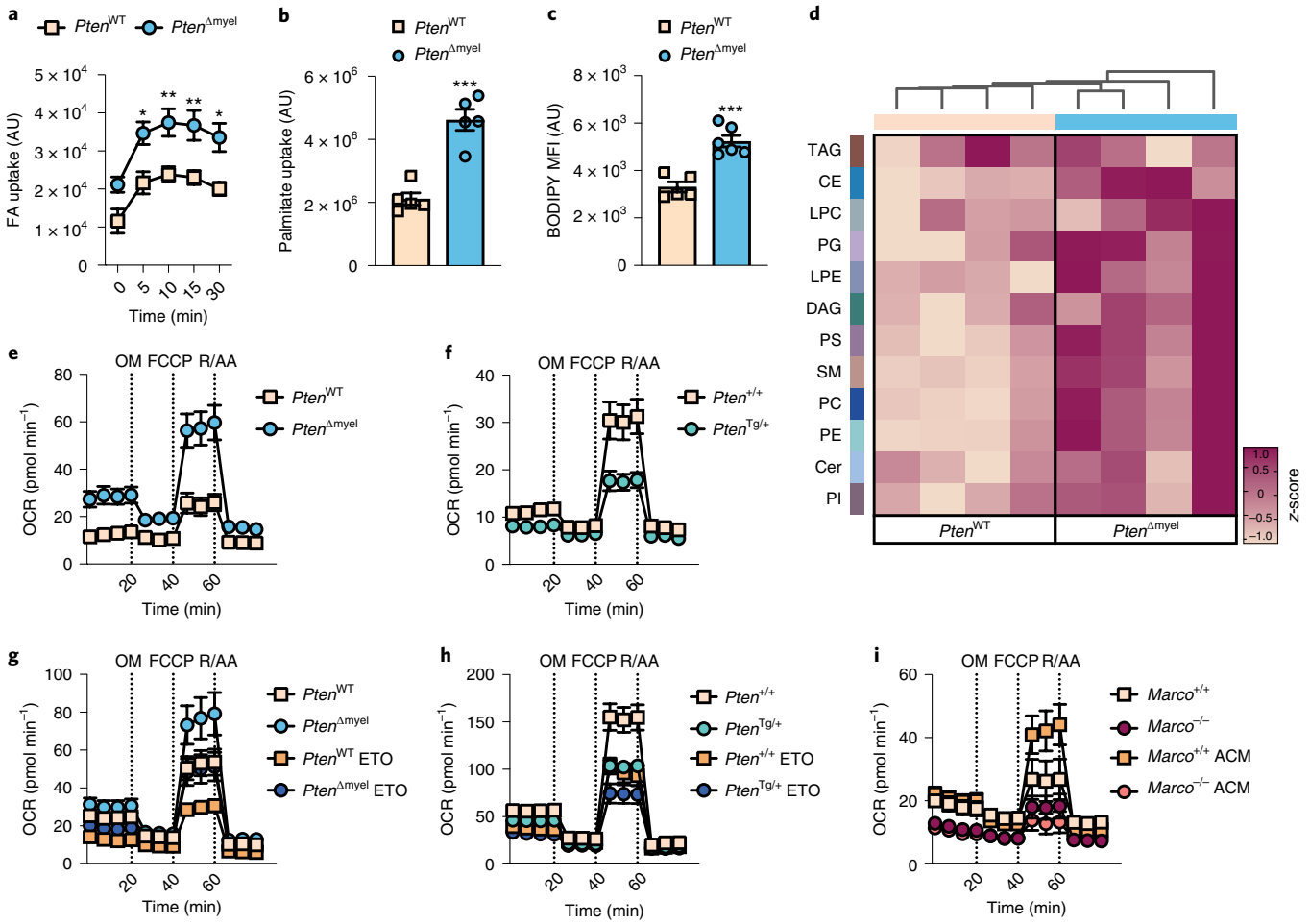

Fig. 7 | PI3K activity sustains myeloid lipid uptake and catabolism. a, Fatty acid uptake of *Pten*^{WT} and *Pten*$^{\Delta myel}$ macrophages ($n=5$ samples; $^{*}P=0.0146$, $^{**}P=0.0096$, $^{**}P=0.0096$, $^{*}P=0.0106$; two-way ANOVA with Bonferroni's correction). **b**, Palmitate uptake of *Pten*^{WT} and *Pten*$^{\Delta myel}$ macrophages ($n=5$ samples; $^{***}P=0.0002$; two-tailed Student's *t*-test). **c**, BODPIY MFI of *Pten*^{WT} ($n=5$ samples) and *Pten*$^{\Delta myel}$ ($n=6$ samples) macrophages ($^{***}P=0.0002$; two-tailed Student's *t*-test). **d**, Differences in intracellular lipid composition between *Pten*^{WT} and *Pten*$^{\Delta myel}$ macrophages ($n=4$ samples). **e**, OXPHOS of *Pten*^{WT} ($n=5$ samples) and *Pten*$^{\Delta myel}$ ($n=8$ samples). **f**, OXPHOS of *Pten*$^{+/+}$ ($n=4$) and *Pten*$^{Tg/+}$ ($n=8$) macrophages; OCR, oxygen consumption rate; OM, oligomycin; FCCP, carbonyl cyanide-*p*-trifluoromethoxyphenylhydrazone; R/AA, rotenone/antimycin A. **g**, OXPHOS of *Pten*^{WT} ($n=13$, + etomoxir (ETO) $n=15$ samples) and *Pten*$^{\Delta myel}$ ($n=15$; + ETO $n=16$ samples) macrophages after 24 h of ETO treatment. **h**, OXPHOS of *Pten*$^{+/+}$ ($n=11$, + ETO $n=12$ samples) and *Pten*$^{Tg/+}$ ($n=11$, + ETO $n=12$ samples) macrophages after 24 h of ETO treatment. **i**, OXPHOS of *Marco*$^{+/+}$ ($n=10$, + ACM $n=12$ samples) and *Marco*$^{-/-}$ ($n=11$, + ACM $n=10$ samples) macrophages after 24 h of ACM treatment. Data are the mean ± s.e.m. and representative of one (**b**, **d**) or two (**a**, **c** and **e**–**i**) independent experiments.

To demonstrate that the beneficial effects of increased lipid buffering mediated by myeloid PI3K were critically linked to the presence of MARCO, we subjected *Pten*$^{\Delta myel}$*Marco*$^{-/-}$ and control animals to a prolonged HFD. Remarkably, increased insulin sensitivity of *Pten*$^{\Delta myel}$ mice was reversed in double-deficient animals (Fig. 8d). As opposed to *Pten*$^{\Delta myel}$ animals, those that were additionally genetically lacking MARCO displayed elevated weight, a phenomenon perhaps connected to their impaired macrophage lipid uptake (Extended Data Fig. 7i). Moreover, improvements in glucose tolerance of *Pten*$^{\Delta myel}$ animals were reversed in double-deficient animals (Fig. 8e and Extended Data Fig. 7j).

Consistent with MARCO-dependent formation of FBC206 ATMs in obesity (Fig. 6f), genetic MARCO deficiency completely revoked the shift in ATM populations characteristic of *Pten*$^{\Delta myel}$ animals (Figs. 4f and 8f). Importantly, double-deficient FBC206 ATMs exhibited significantly less intracellular lipids than *Pten*$^{\Delta myel}$ animals (Fig. 8g). Verifying the proposition of myeloid PI3K-driven lipid buffering, serum lipid profiling of *Pten*$^{\Delta myel}$ animals revealed an overall decrease in lipid species that was largely reversed in double-deficient animals (Fig. 8h; black dotted line). In accordance with robust intracellular lipid accumulation of PCs, PEs and PSs in ACM-challenged *Pten*$^{\Delta myel}$ macrophages (Fig. 8c; blue ribbon) after HFD feeding, these species were markedly decreased in the serum of *Pten*$^{\Delta myel}$ animals (Fig. 8h; bold lines). Consistent with these same lipids being scavenged by macrophages dependent on PI3K and MARCO (Fig. 8c), their abundance was higher in obese *Pten*$^{\Delta myel}$*Marco*$^{-/-}$ relative to *Pten*$^{\Delta myel}$ animals (Fig. 8h). This was also true for metabolically detrimental serum ceramides[41] (Fig. 8h). Further, LPC and LPE levels, previously shown to accumulate under ACM stimulation in double-deficient macrophages, were selectively increased in *Pten*$^{\Delta myel}$*Marco*$^{-/-}$ mice, while remaining unchanged in *Pten*$^{\Delta myel}$ mice.

Together, these data demonstrate that, in obesity, myeloid PI3K activity exerts protective effects on metabolic health by inducing a FBC206 ATM population with a high lipid-buffering capacity that prevents ectopic lipid spillover in a MARCO-dependent manner (Fig. 8i).

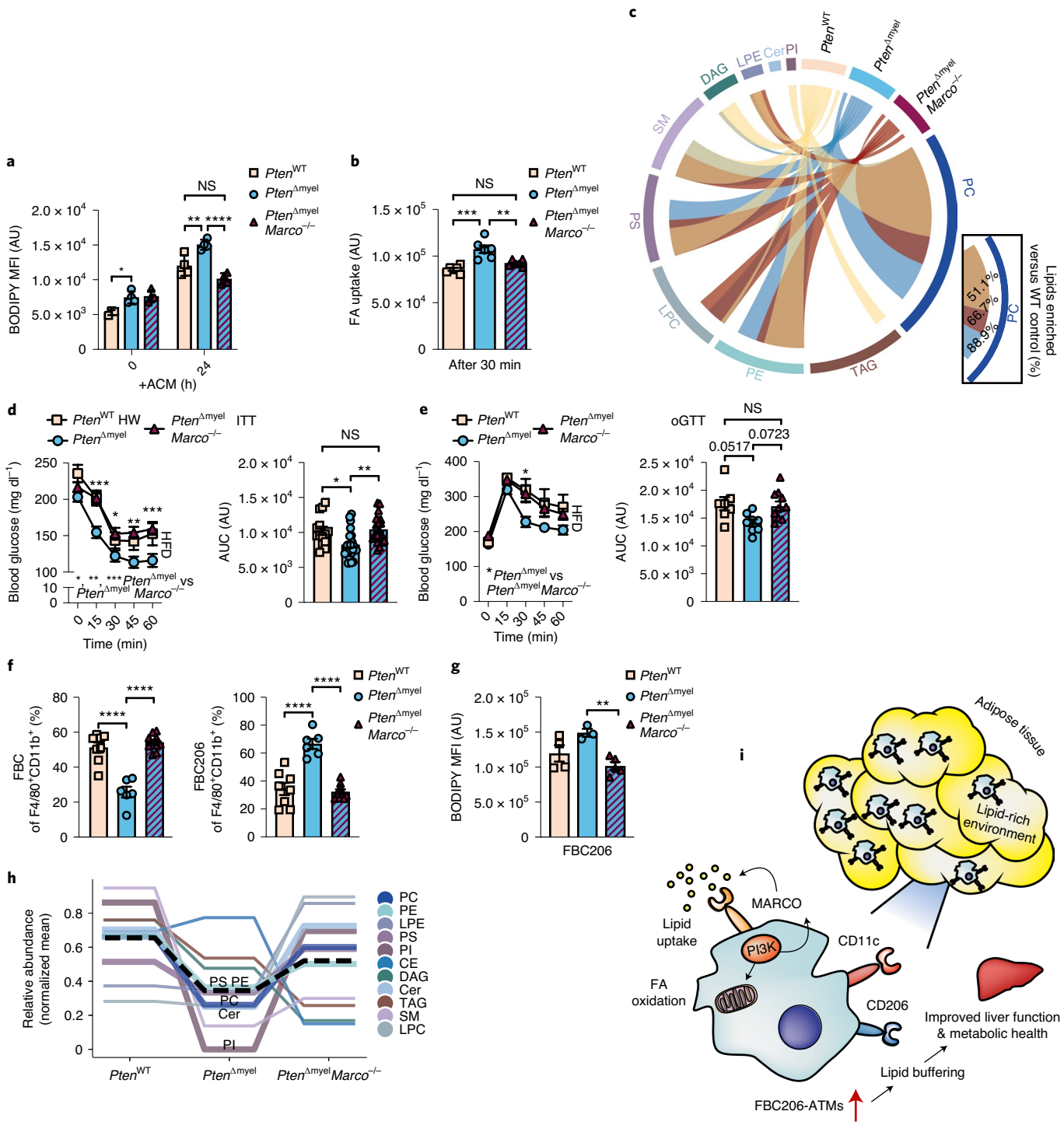

Fig. 8 | Beneficial effects of myeloid PI3K in diet-induced obesity are dependent on MARCO. a, MFI of BODIPY after ACM treatment of *Pten*^{WT}, *Pten*$^{\Delta myel}$ and *Pten*$^{\Delta myel}$*Marco*$^{-/-}$ macrophages ($n=4$ samples; $^{*}P=0.0404$, $^{**}P=0.0014$ and $^{****}P<0.0001$; two-way ANOVA with Bonferroni's correction). **b**, Fatty acid uptake of *Pten*^{WT}, *Pten*$^{\Delta myel}$ and *Pten*$^{\Delta myel}$ *Marco*$^{-/-}$ macrophages ($n=5$ samples; $^{***}P=0.0001$ and $^{**}P=0.0039$; one-way ANOVA with Bonferroni's correction). **c**, Intracellular lipid enrichment of *Pten*^{WT}, *Pten*$^{\Delta myel}$ and *Pten*$^{\Delta myel}$*Marco*$^{-/-}$ macrophages after 24 h of ACM treatment ($n=4$ samples; for *Pten*^{WT} ACM $n=3$); Cer, ceramide. **d**, ITT and AUC after 16 weeks' feeding of *Pten*^{WT} (HW; $n=14$), *Pten*$^{\Delta myel}$ ($n=23$) and *Pten*$^{\Delta myel}$*Marco*$^{-/-}$ ($n=21$; $^{***}P=0.0002$, $^{*}P=0.0333$, $^{**}P=0.0018$, $^{***}P=0.0007$, two-way ANOVA with Bonferroni's correction; $^{*}P$ for AUC = 0.0142 and $^{**}P$ for AUC = 0.0019, one-way ANOVA with Bonferroni's correction). **e**, oGTT and AUC of *Pten*^{WT} ($n=7$), *Pten*$^{\Delta myel}$ ($n=8$) and *Pten*$^{\Delta myel}$*Marco*$^{-/-}$ ($n=10$) mice 16 weeks after HFD feeding ($^{*}P=0.0428$; two-way ANOVA with Bonferroni's correction; one-way ANOVA with Bonferroni's correction for AUC). **f**, FBC and FBC206 levels in eWAT of *Pten*^{WT} ($n=6$), *Pten*$^{\Delta myel}$ ($n=9$) or *Pten*$^{\Delta myel}$*Marco*$^{-/-}$ ($n=8$) animals 16 weeks after HFD. Cells were gated on viable CD45^{+}CD11b^{+}F4/80^{+} ($^{****}P<0.0001$; one-way ANOVA with Bonferroni's correction). **g**, BODIPY MFI of *Pten*^{WT} ($n=4$), *Pten*$^{\Delta myel}$ ($n=3$) and *Pten*$^{\Delta myel}$*Marco*$^{-/-}$ ($n=5$) FBC206 ATM population 16 weeks after HFD. Cells were gated on viable CD45^{+}CD11b^{+}F4/80^{+}CD11c^{+}CD206^{+} ($^{**}P=0.0088$; one-way ANOVA with Bonferroni's correction). **h**, Genotype- dependent changes of relative abundance in serum lipid components 16 weeks after HFD ($n=4$ *Pten*^{WT}, $n=4$ *Pten*$^{\Delta myel}$ and $n=5$ *Pten*$^{\Delta myel}$*Marco*$^{-/-}$ animals). **i**, Schematic illustrating the influence of PI3K on lipid-buffering FBC206 ATMs in obesity. Data are the mean ± s.e.m. and representative of one (**b**, **c**, **g** and **h**), two (**a**) or are pooled from two (**e** and **f**) or six (**d**) independent experiments.

Discussion

Exhausted adipose expansion coinciding with ectopic lipid spillover are common features of metabolic syndrome and hallmarks of unhealthy obesity[1]. ATMs drastically accumulate in obesity, but are heterogeneous, exerting both beneficial and detrimental effects[3,7,10,11]. The molecular triggers and signalling pathways governing this heterogeneity are incompletely understood. Here, we show myeloid PI3K signalling promotes a metabolically beneficial ATM population defined by the markers F4/80, CD11b, CD11c and CD206 (FBC206) that is critically characterized by high MARCO surface expression, which sustains macrophage lipid uptake and intracellular lipid metabolism.

Previous studies have demonstrated that FBC ATMs are derived from the circulation, constituting the majority of increased ATM content in obesity[10,42]. CD206 is a marker for alternatively activated ATMs, predominantly expressed by FB ATMs in the lean state[3,43]. We demonstrate that, in acute lipolysis, FBC206 ATMs are richest in intracellular lipids and lysosomes as compared to FB and FBC ATM populations. Further, following a ST-HFD, these cells display the highest TREM-2 levels and expression of CD9, two markers for obesity-induced lipid-associated macrophages, exhibiting lysosomal and phagocytic transcription[6,7]. Although in acute lipolysis resident FBC206 ATMs most efficiently buffer lipids, it is highly likely that substantial proportions of them are derived from the circulation during prolonged obesity. Regardless, we propose that FBC206 ATMs are shaped by a metabolically stressed environment to handle, store and catabolize incoming lipids more efficiently, thereby maintaining insulin sensitivity and glucose tolerance.

In obesity, ATMs contribute to systemic metabolically triggered inflammation and are exposed to a microenvironment rich in lipids, cytokines, chemokines and adipokines[3,4,13]. While ACM and free fatty acid treatment of naïve macrophages induced lipid-laden FBC206-expressing cells, any of the single cytokines, adipokines or lipids tested here did not. Interestingly, leptin induces lipid-laden macrophages via dependency on PI3K, and both TNF-α and IL-1β reportedly promote lipid retention in pre-lipid-laden macrophages[44,45]. Although complex mixtures of free fatty acids are clearly an upstream signal for FBC206 generation, we hypothesize that synergy between cytokines and lipids might be critical for the generation of these cells. Nonetheless, we demonstrate that PI3K triggers their generation, functionality and elevates their MARCO levels. Further, our data suggest the existence of a feed-forward loop in which MARCO-dependent lipid uptake facilitates FBC206 generation. In line with this, enhanced FBC206 ATM presence in obese animals possessing myeloid cells with augmented PI3K activity is reversed by MARCO deficiency.

Our findings add another layer to the fundamental role of PI3K–AKT signalling in metabolic health, which is predominantly ascribed to the insulin-dependent regulation of glucose and lipid metabolism. PI3K downregulation is implicated in metabolic dysfunctions and obesity-induced insulin resistance[17–19]. Supporting this, several studies have demonstrated that deletion of the PI3K-antagonizing PTEN in liver, adipose, muscle and pancreatic beta cells improves glucose tolerance and insulin sensitivity by directly facilitating insulin-induced PI3K signalling[20–23]. In obese humans, PTEN haploinsufficiency is associated with profound insulin sensitization[46]. Similarly, here we show that myeloid PTEN deficiency improves metabolic health in obesity. Macrophages are considered insulin sensitive, and in the postprandial state, IL-1β promotes insulin secretion[47]. Although, there were no differences in ATM IL-1β levels in $Pten^{Tg/+}$>WT animals compared to controls, we cannot exclude contributions of decreased serum cytokines to their attenuated insulin secretion following glucose gavage. Notably, rather than displaying expected profound insulin resistance, obese mice that are deficient for the insulin receptor on myeloid cells exhibit improved insulin sensitivity[48]. Thus, the beneficial metabolic effects of augmenting PI3K action in myeloid cells are unlikely directly connected to improved PI3K-dependent ATM-intrinsic insulin signalling. Following disruption of adipose tissue homeostasis, we observed p-AKT loss in the total ATM pool, reminiscent of macrophage insulin resistance. Nonetheless, we demonstrate that FBC206 ATMs display conserved p-AKT as they preserve their cell-intrinsic PI3K signalling, which we show sustains lipid uptake and metabolism. Future studies are required to determine whether PI3K signalling influences this population in humans[31]. Therefore, although moderate pharmacological PI3K inhibition might be a therapeutic strategy for obesity and metabolic syndrome[49], it could also be associated with unforeseen effects on the ATM compartment and dyslipidaemia.

Counterintuitively, insulin-resistant macrophages upregulate scavenger receptors, including CD36 and scavenger receptor A, partly via receptor shuttling and degradation defects[50,51]. Scavenger receptors bind and engulf modified lipids[36]. Although extensively studied in atherosclerosis[52], scavenger receptor-mediated lipid engulfment has achieved less attention in studies of obesity. Initial work showed that alveolar macrophages expressed MARCO scavenged bacteria and modified lipids[53,54]. This and its hepatic upregulation in obese mice[55] are contributing to the evidence for MARCO potentially facilitating lipid uptake. Here, we demonstrate that MARCO-deficient macrophages display reduced lipid uptake and that MARCO buffers lipids in acute lipolysis, preventing NEFA elevations and hypoglycaemia. In contrast to shorter HFD feeding[56], long-term HFD-fed MARCO-deficient animals displayed insulin resistance and glucose intolerance, associated with decreased lipid content in their FBC206 ATMs. The exact mechanisms of MARCO-dependent intracellular lipid accumulation remain to be elucidated, although they may involve macropinocytosis and/or endocytosis, as these pathways regulate MARCO internalization[57]. Critically, we demonstrate that PI3K activity upstream of NRF2 activation increases myeloid MARCO surface expression and genetically deleting MARCO in $Pten^{\Delta myel}$ animals reversed their improved insulin sensitivity and glucose tolerance in obesity. Lipidomic analysis of ACM-challenged macrophages confirmed that enhanced lipid buffering mediated by PTEN-deficient macrophages relied on their increased MARCO levels. Lipids internalized in macrophages through dependency on MARCO were higher in the serum of HFD-fed $Pten^{\Delta myel}Marco^{-/-}$ animals than HFD-fed $Pten^{\Delta myel}$ animals. Although these data provide compelling evidence that sustained PI3K activity in macrophages prevents lipotoxicity, PI3K-induced MARCO-dependent lipid diversion into FBC206 ATMs might not solely be responsible for the health improvements of obese $Pten^{\Delta myel}$ animals. Hypothetically, other beneficial functions of MARCO, including its postulated roles in apoptotic cell clearance[58,59], might also contribute in a PI3K- and MARCO-dependent manner.

As the contributions of macrophages in obesity are still under debate, there is an urgent need for a better understanding of the pathways governing beneficial versus detrimental ATM actions. We propose that improved myeloid metabolic fitness through increased lipid scavenging and enhanced energy metabolism contributes to the preservation of systemic metabolic health. Concordantly, defects in macrophage OXPHOS are reportedly associated with increased insulin resistance in obesity[60]. Our results highlight contributions of myeloid PI3K signalling herein, describing a mechanism whereby cell-intrinsic PI3K signalling boosts beneficial ATM phenotypes characterized by elevated MARCO-dependent myeloid lipid uptake.

Methods

Experimental animals. Mice were bred and housed in pathogen-free facilities at the Medical University of Vienna and kept in a 12-h light cycle, at 21–23 °C and 45–65% humidity in cages with a maximum of four male and five female animals per cage. All experimental procedures were approved by the Austrian Ministry of Sciences under the project numbers 66.009/0066-WF/V/3b/2016,

66.009/0097-WF/V/3b/2017, 66.009/0377-V/3b/2019 and 66.009/0264-V/3b/2019 and were conducted in strict accordance with Austrian law. Animal experiments performed in Australia were granted permission under project number 17-04 at the Garvan and St. Vincent's Ethics Committee. WT mice were on the C57BL/6J background and purchased from Charles River Laboratories (JAX mice strain 632). *Pten*$^{loxP/loxP}$*LysM*-Cre$^{+/-}$ (Mouse Genome Informatics (MGI) nos. 2182005 and 1934631; *Pten*$^{\Delta myel}$) mice were backcrossed to a C57BL/6J background for at least eight generations[30]. For deletion efficiency experiments, *Pten*$^{\Delta myel}$ were further crossed to R26^{tdTomato} mice (C57BL/6J background; MGI 3813512), which were a kind gift from C. Österreicher[34]. *Pten*$^{Tg/+}$ mice (MGI 5645732) on a C57BL6/CBA background were supplied by the laboratory of M. Serrano[26] and bred with C57BL/6J females (at least for five generations). The resulting 8- to 12-week-old male mice were used as donors for BMTs. *Marco*$^{-/-}$ mice (C57BL/6 background, MGI 1309998) were backcrossed for at least five generations to a C57BL/6J background and were a kind gift from K. Tryggvason[61]. *Pten*$^{\Delta myel}$ and *Marco*$^{-/-}$ were intercrossed in-house to generate *Pten* and *Marco* double-deficient mice (*Pten*$^{\Delta myel}$*Marco*$^{-/-}$). *Nrf2*$^{-/-}$ mice[62] (C57BL/6 background; Riken BRC, RBRC01390) were kindly provided by M. Yamamoto and F. Gruber. *Ccr2*$^{gfp/gfp}$ mice were bought from the Jackson Laboratory (027619). *PI3Kγ*$^{KD/KD}$ (C57BL/6J background, MGI 3051886) mice were kindly provided by E. Hirsch[39]. *Akt1*$^{loxP/loxP}$ *Akt2*$^{loxP/loxP}$*LysM*-Cre$^{+/-}$ mice (C57BL/6J background; Jackson Laboratory, 026474 and 026475) were a kind gift from C. Tsatsanis.

Eight- to twelve-week-old sex- and age-matched littermates were used for in vitro approaches. For in vivo experiments, eight- to twelve-week-old age-matched male mice and their respective littermate controls were used unless otherwise stated. Mice were maintained on a normal chow diet (Ssniff, V1536). Dietary interventions commenced at 6 weeks of age using a diet that contained 60% calories from fat (Research Diets, D12492), or for ND studies, mice were maintained on the chow diet (Ssniff, V1536). Lean body mass and fat mass were measured using a 4-in-1 EchoMRI body composition analyser (Columbus Instruments). For in vivo lipid uptake experiments, animals were intraperitoneally injected with 50 µg BODIPY FL C16 (Thermo Fisher Scientific, D3821), and adipose tissue was harvested after 1 h.

Bone marrow transplantations. Bone marrow from *Pten*$^{Tg/+}$ animals and littermates was isolated by flushing out cells from the femur and tibia with sterile RPMI. Lethally irradiated (9 Gy) 6-week-old WT C57BL/6J recipient mice were injected retro-orbitally with 2×10^6 cells under anaesthesia and were allowed to recover for 5–6 weeks on chow diet. As a control, some mice were reconstituted with CD45.1 bone marrow, and chimerism was confirmed by flow cytometry of the blood. After recovery, mice were given a high fat diet (Research Diets, D12492).

Intraperitoneal insulin and oral glucose tolerance tests. Mice were starved for 2 h (ITT) or 5 h (GTT), after which body weight and basal blood glucose levels were measured. Mice were injected with 0.1 U human insulin per gram of body weight (0.1 U ml^{-1} diluted in 0.9% NaCl; ITT) or gavaged with 20% glucose (1 g kg^{-1}; GTT). Blood glucose was measured 15, 30, 45 and 60 min after insulin/glucose administration via tail vein puncture using an Accu-Chek glucometer in combination with Accu Check Go Test Strips (Roche, 05182913).

Hyperinsulinaemic-euglycaemic clamps. After 16 weeks of HFD feeding of *Pten*$^{Tg/+}$ > WT and *Pten*$^{+/+}$ > WT animals, dual-cannulation surgery was performed under aseptic conditions with general anaesthesia (4% isoflurane for induction; 1.5–2% maintenance). Catheters were inserted into the left carotid artery and right jugular vein[63] and, after a 5–7 d recovery period during which weights were monitored and catheters flushed every 1–2 d, hyperinsulinaemic-euglycaemic clamps were performed[63,64]. After 5 h of fasting, animals received a [3-^{3}H]glucose (0.05 mCi min^{-1}) infusion for 90 min to facilitate the calculation of basal hepatic glucose production and whole-body glucose uptake. The hyperinsulinaemic clamp was then initiated with all mice getting the same dose of insulin (24 mU kg^{-1} bolus followed by 6 mU kg min^{-1} continuous infusion; based on a 30 g mouse) and the rate of [3-^{3}H]glucose infusion was increased to 0.1 mCi min^{-1}. Euglycaemia (8 mM) was maintained during the clamp by measuring blood glucose every 10 min and infusing 25% glucose as necessary. At the end of the clamp, animals were euthanized. The rate of basal and clamp glucose disappearance was determined using steady-state equations. Clamp hepatic glucose output was determined by subtracting the glucose infusion rate from glucose disappearance.

Acute lipolysis induced by CL316,243 treatment. Indicated mice were intraperitoneally injected with 1 mg kg^{-1} of CL316,243 (Sigma-Aldrich, C5976) or with NaCl. Subsequently, blood glucose was measured using an Accu-Chek glucometer in combination with Accu Check Go Test Strips (Roche, 05182913) at 1, 2, 3 and 4 h after CL316,243 administration, and 5 µl of blood was drawn via tail vein puncture. Plasma NEFA levels were measured according to the manufacturer's instructions (Wako Chemicals). For SVF isolation and subsequent flow cytometric analysis, mice were injected twice at 18 h and 14 h before the harvest with 1 mg kg^{-1} CL316,243.

Mouse laboratory parameters and ELISAs. Serum alanine transaminase, aspartate transaminase and triglycerides were quantified with tests certified for in vitro diagnostics at the Department of Biomedicine Research of the Medical University of Vienna. Plasma insulin levels were determined using the Ultrasensitive Mouse Insulin ELISA kit from Mercodia (10-1249-01) or Alpco (80-INSMSU-E01). C-peptide levels were determined using Mouse C-peptide ELISA Kit (Crystal Chem, 90050). Free fatty acids were measured in plasma or cellular supernatants using the NEFA kit according to the supplier (Wako Chemicals, 91795 and 91995). Glycerol levels were determined by using free glycerol reagent (Sigma-Aldrich, F6428) according to the manufacturer's instructions. Wavelengths were assessed using Gen5 1.11 software on a Synergy H4 machine (BioTek).

Organ weights, histology and steatosis scoring. Following harvest, livers and adipose depots were weighed. Murine fat mass corresponds to combined weights of anterior, posterior, perigonadal (eWAT), retroperitoneal (rWAT) and mesenteric fat depots. Livers were fixed in 4% formaldehyde, embedded in paraffin, cut in 2-µM sections and stained using H&E. Images of stained sections were examined in bright field and acquired using the Olympus FSX100 all-in-one microscope system and FSX-BSW (02.02) software at ×20 magnification. Liver steatosis was scored by a blinded, experienced pathologist on H&E sections. Macrovesicular steatosis and microvesicular steatosis were both separately scored and graded from 0–100%. Steatosis was defined by whether the vacuoles displaced the nucleus to the side (macrovesicular) or not (microvesicular).

Ex vivo lipolysis. Murine epididymal fat pads were harvested and cut into 50-mg pieces. Pieces were individually placed into 500 µl of phenol red-free DMEM containing 2% FA-free BSA (Sigma-Aldrich, A8806) with or without 1 µM isoproterenol (Sigma-Aldrich, I6504) at 37 °C for 2 h. Subsequently, NEFAs were measured according to the manufacturer's instructions (Wako Chemicals).

Peritoneal macrophage isolation and culture. Animals were killed by cervical dislocation and the peritoneal cavity was flushed with sterile 1× PBS. Cells were plated, washed after 3 h and supplemented with complete RPMI (10% FBS and 1% penicillin–streptomycin). On the following day, cells were stimulated as indicated and the following reagents and their concentrations were used: etomoxir, 100 µM (Sigma-Aldrich, E1905); wortmannin, 200 nM (Sigma-Aldrich, W1628); glucose, 30 mM (Thermo Fisher, A2494001); insulin, 10 nM (Sigma-Aldrich, I6643); fatty acid supplement, 5 µl ml^{-1} (Sigma-Aldrich, F7050); murine IL-6, 10 ng ml^{-1} (PeproTech, 216-16); murine IL-1β, 10 ng ml^{-1} (PeproTech, 211-11B); murine TNF-α, 10 ng ml^{-1} (PeproTech, 315-01A); murine leptin, 20 nM (PeproTech, 450-31); murine adiponectin (PeproTech, 315-26); 1 µg ml^{-1} Seahorse XF Palmitate-BSA FAO Substrate 400 µM (Agilent Technologies, 102720); 0.5 µl ml^{-1} Oleic Acid-Albumin (Sigma, O3008); 4 µl ml^{-1} cholesterol lipid concentrate (LifeTech, 12531018); insulin, 10 nM (Sigma, I-6634); glucose, 30 mM (Sigma-Aldrich, G8644); duvelisib, 500 nM (MedChemExpress, HY-17044); brusatol, 40 nM (Sigma-Aldrich, SML1868); and resatorvid, 10 nM (MedChemExpress, HY-11109). For flow cytometry, cells were detached using Enzyme Free (Milipore, S-014-B) and subsequently stained (see below). For RNA isolation, macrophages were harvested in TriFast (Peqlab, 30-2010).

Adipocyte differentiation. E12.5 pregnant WT and *Marco*$^{-/-}$ animals were euthanized, embryos removed and placed into 10 ml of 1× PBS. Embryos were isolated, their heads removed and cut into fine and homogenous pieces. The resulting cell suspension was incubated overnight at 37 °C and 5% CO_2 in DMEM supplemented with 10% FBS and 1% penicillin–streptomycin (Sigma-Aldrich, D5796). Subsequently, medium was exchanged. Next, 48 h after isolation, cells were harvested using trypsin and split into a 15-cm dish. Primary mouse embryonic fibroblast cells (passage 3–8) were harvested at 80% confluence with 1× trypsin (Gibco, 15090-046). Preadipocytes were differentiated for 14 d by changing the medium to full medium containing 5 µg ml^{-1} insulin (Sigma, I3536), 5 µM troglitazone (Sigma, T2573), 0.5 mM isobutylmethylxanthine (Sigma, I5879) and 1 µM dexamethasone (Sigma, D8893). After 48 h, the medium was again exchanged to medium supplied with 5 µg ml^{-1} insulin and 5 µM thiazolidinedione. Medium containing insulin and thiazolidinedione was renewed every 3–4 d. After differentiation, cells were harvested in TriFast (Peqlab, 30-2010).

Stromal vascular fraction isolation. Epididymal fat pads were harvested from indicated animals, cut into small pieces and washed twice with DMEM/F12 medium (Gibco, 11320-074) followed by centrifugation for 8 min at 500*g* at room temperature. Digestion was carried out in 10 ml of freshly prepared collagenase II solution (1 mg ml^{-1} in 1.5% sterile BSA, in DMEM/F12) at 37 °C for 1 h. Subsequently, 100 µl of 0.5 M EDTA was added and the digested adipose–enzyme solution was filtered through a 100-µm strainer into 20 ml of DMEM/F12 medium supplemented with 10% FBS and centrifuged as previously. After centrifugation, the pellet was washed twice and resuspended in 1 ml of erythrocyte lysis buffer (Qiagen, 79217) for 5 min, after which 12 ml of medium was added. The resulting cell suspension was counted, centrifuged and further stained for flow cytometric analysis.

Isolation of liver mononuclear cells. Livers were perfused with HBSS via the portal vein, cut into small pieces and digested in RPMI containing 0.05% collagenase/dispase (Roche, 10269638001) and 0.01% trypsin inhibitor (Thermo Fisher Scientific, 17075029) for 1 h at 37 °C. The resulting liver suspension was passed through a 40-µm cell strainer, centrifuged at 800*g* (10 min at 4 °C), and the cell pellet was resuspended in 10 ml RPMI. Cell suspensions were overlayed onto 15 ml of 33% (vol/vol) Percoll solution (Sigma-Aldrich, P1644) and centrifuged for 30 min at room temperature with no brake. The supernatant was removed and erythrocytes were lysed by resuspending the pellet in 2 ml of red blood cell lysis buffer for 4 min, after which 8 ml of RPMI was added. Cell suspensions were spun at 800*g* (5–10 min at 4 °C), supernatant removed, and the cells were washed twice with 10 ml RPMI. Cells were subsequently resuspended in PBS/2% FBS and total cell numbers for each liver were enumerated using a haemocytometer (Turck chamber) before staining for flow cytometry.

Quantitative PCR with reverse transcription. Total RNA was extracted from cells using RNA isolation kits (TriFast and Peqlab, 30-2010). Reverse transcription was performed using commercially available kits (Applied Biosystems) and Luna Universal quantitative PCR (qPCR) Master Mix (New England Biolabs, M3003E) for the qPCR reaction. Water controls and postamplification melting curve analysis were included to ensure absence of primer dimers. qPCRs were performed on a Step-OnePlus (Applied Biosystems) using Step-OnePlus Real-Time PCR Software (v.2.3). Data are shown as the fold change. Normalization to hypoxanthine phosphoribosyltransferase 1 (*Hprt*) or, in Fig. 1i and Fig. 2g, to eukaryotic translation elongation factor 1 Alpha 1 (*Eef1a1*) within each sample was performed. Then, $2^{-\Delta\Delta Ct}$ values were calculated ($\Delta\Delta Ct = \Delta Ct$ treatment $- \Delta Ct$ control). RT–PCR was performed using the following primers: *Hprt*: 5′-CGC AGT CCC AGC GTC GTG-3′ and 5′-CCA TCT CCT TCA TGA CAT CTC GAG-3′; *Marco*: 5′-TGA TGC GAC TGT CTT CTG TCG and 3′-CAT TGT CCA GCC AGA TGT TCC-5′; *Pten*: 5′-ACA CCG CCA AAT TTA ACT GC-3′ and 3′-TAC ACC AGT CCG TCC CTT TC-5′; *Tnf*: 5′-CCA CCA CGC TCT TCT GTC TAC-3′ and 3′-AG GGT CTG GGC CAT AGA ACT-5′; *Il6*: 5′-CAA GTC GGA GGC TTA ATT ACA CAT G-3′ and 3′-ATT GCC ATT GCA CAA CTC TTT TCT-5′; *Il1b*: 5′-GGA CAG AAT ATC AAC CAA CAA GTG ATA-3′ and 3′-GTG TGC CGT CTT TCA TTA CAC AG-5′; *Ppargc1a*: 5′-CCG ATC ACC ATA TTC CAG GT-3′ and 3′-GTG TGC GGT GTC TGT AGT GG-3′; *Ppargc1b*: 5′-CTC CAG GCA GGT TCA ACC C-3′ and 3′-GGG CCA GAA GTT CCC TTA GG-5′; *Cpt1a*: 5′-GGT CTT CTC GGG TCG AAA GC-3′ and 3′-TCC TCC CAC CAG TCA CTC AC-5′; *Cpt1b*: 5′-CAA GTC ATG GTG GGC AAC TA-3′ and 3′-GCT GCT TGC ACA TTT GTG TT-5′; *Ppar-γ*: 5′-ACC CAG AGC ATG GTG CCT TCG C-3′ and 3′-CCG AAG TTG GTG GGC CAG AAT GGC A-5′; *Eef1a1*: 5′-CTG CGT TTT GGT CAC TAC TCA GG-5′ and 3′-TCC ACA GGC AGC AAA CAG TG-5′; *Srebf1*: 5′-GCA TGC CAT GGG CAA GTA C-3′ and 3′TGT TGC CAT GGA GAT AGC ATC T-5′; *Cd36*: 5′-GGA GCA ACT GGT GGA TGG TT-3′ and 3′-TTG AGA CTC TGA AAG GAT CAG CA-5′; *Fasn*: 5′-GGA GGT GGT GAT AGC CGG TAT-3′ and 3′-TGG GTA ATC CAT AGA GCC CAG-5′; *Acaca*: 5′-TTG AGA AGG TTC TTA TCG CCA AC-3′ and 3′-GAC CAC CGA CGG ATA GAT CG-5′; *Acacb*: 5′-TCC GTA ATG AAC GTG CCA TC-3′ and 3′-CAT CTT GAT GTA CTC TGC GTT GG-5′; *Cd68*: 5′-TGG CGC AGA ATT CAT CTC TTC-3′ and 3′-GGT CAA GGT GAA CAG CTG GAG-5′; *Ndufs1*: 5′-TTG GGA ACA ACA GGA AGA GG-3′ and 3′-TTC CCA CTG CAT CCA TTA CA-5′; *Sdhd*: 5′-CTG GTG GAA CGG AGA CAA GT-3′ and 3′-GTT AAG CCA ATG CTC GCT TC-5′; *Uqcr11*: 5′-TCC AAC AAC TTG GGA ACC TC-3′ and 3′-GGT GCT GTG GTG ACA TTG AG-5′; *Cox7c*: 5′-AGA ACT TCC AGC AGC GAC AT-3′ and 3′-TAA AGA AAG GTG CGG CAA AC-5′; *Atp5me*: 5′-CGG TTC AGG TCT CTC CAC TC-3′ and 3′-TGA CGC CTC ACT TGA GAA TG-5′.

Flow cytometry and cell sorting. Adherent peritoneal macrophages or freshly isolated SVF cells were resuspended in cold PBS/1% FBS and stained with fixable viability dye (Invitrogen, 65-0865-14) or 7-AAD (SYTOX AADvanced Dead Cell Stain; Invitrogen, S10274) for dead-cell detection. The following antibodies and their dilutions were used: CD45.2-BV650 (Clone 104; BioLegend, 109836; 1:100), CD45-V500 (Clone 30-F11; BD Horizon, 561487; 1:100), F4/80-BV605 (Clone BM8; BioLegend, 123133; 1:80), F4/80-FITC (Clone BM8; BioLegend, 123108; 1:100), CD11b-PeCy7 (Clone M1/70; eBioscience, 25-0112; 1:500), CD11b-PB (Clone M1/70; Invitrogen, RM2828; 1:100), CD11c-APC-eF780 (Clone N418; eBioscience, 47-0114; 1:100), CD11c-PC5.5 (Clone N418; eBioscience, 35-0114-82; 1:80), CD206-AF700 (Clone C068C2; BioLegend, 141733; 1:200), CD206-PE (Clone C068C2; BioLegend, 141705; 1:100), MARCO-APC (Clone 579511; R&D, FAB2956A; 1:25), MARCO-PE (Clone ED31; Invitrogen, 15225929; 1:50), CD9-PE (Clone MZ3; BioLegend, 124805; 1:200), TREM-2-PE (Clone 237920; R&D, FAB17291P; 1:15), Ly6G-AF700 (Clone 1A8; BioLegend, 127622; 1:200), Ly6C-BV605 (Clone HK1.4; BioLegend, 128035; 1:80), Ly6C-PE/Cy7 (Clone HK1.4; BioLegend, 128017; 1:100), B220-PE-Cy5 (Clone RA3-6B2; Tonbo, 55-0452; 1:80), CD3-PerCP-Cy5.5 (Clone 145-2C11; Tonbo, 65-0031; 1:80), CD3-APC (Clone 17A2; eBioscience, 17-0032-82; 1:160), CD19-BV605 (Clone 6D5; BioLegend, 115540; 1:200), CD4-AF700 (Clone RM4-5; eBioscience, 56-0042-82; 1:100) and CD8-Pe/Cy7 (Clone 53-6.7; BioLegend, 100721; 1:200). Intracellular staining was performed using the fixation and permeabilization buffer set (eBioscience, 88-8824-00) or True-Phos Buffer Set (Biolegend, 425401) according to the manufacturer's instructions and included p-AKT-APC (Clone SDRNR; eBioscience, 17-9715-42; 1:50) and PTEN-BV421 (Clone A2B1; BD, 566637; 1:30) or isotype control mouse IgG2a-APC (Clone eBM2a; eBioscience, 17-4724-81; 1:50) and mouse IgG1k-BV421 (Clone X40; BD, 562438; 1:30). Mitochondria and lysosomes were assessed by staining the cells with MitoTracker Green (Thermo Fisher, M7514) and LysoTracker Deep Red (Life Technologies, L12492) as recommended by the manufacturers. Assessment of lipid content was performed by incubation of cells with BODIPY 493/503 (Fisher Scientific, 11540326) for 15 to 30 min at 37 °C. Uptake of differentially labelled lipid species was assessed by incubating peritoneal macrophages with AcLDL-Alexa Fluor 488 (Fisher Scientific, 10287482) or BODIPY-C16 in complete RPMI for the indicated amount of time.

For flow cytometric analysis of blood monocytes, EDTA-treated blood was stained with antibodies and subsequently fixed with 2% PFA for 15 min. The cell suspension was further subjected to red blood cell lysis before processing for intracellular staining or flow cytometric analysis. For cell sorting, murine ATMs were filtered through a 40-µM cell strainer and sorted as live, $CD45^+CD3^-CD11b^+F4/80^+CD11c^+CD206^{+/-}$ on a FACSAria II flow cytometer (BD). Stained cells were analysed on the FACSCalibur (BD), LSRFortessa (BD) and CytoFLEX S Flow Cytometer (Beckman Coulter) and analysed using CytExpert (v.2.0) and FlowJo (v.10).

Adipocyte conditioned media generation. For ACM preparation, epididymal fat pads were harvested from animals after 18 weeks of HFD feeding, cut into small pieces and washed twice with DMEM/F12 medium (Gibco, 11320-074) by centrifugation for 8 min at 500*g* at room temperature. Digestion was carried out in freshly prepared collagenase II solution as for the SVF isolation described previously. Subsequently, the digested adipose–enzyme solution was filtered through a 100-µm strainer into 20 ml DMEM/F12 medium supplemented with 10% FBS and centrifuged. Floating mature adipocytes were harvested and plated on a 10-cm Petri dish in 10 ml of serum-free DMEM/F12. On the next day, medium containing cells was filtered through a 40-µm cell strainer, aliquoted and stored at −20 °C. For in vitro ACM stimulations of macrophages, medium was changed to ACM diluted at 1:5 in RPMI for the indicated amount of time.

Fatty acid uptake. Peritoneal macrophage fatty acid uptake was performed using the Free Fatty Uptake Assay Kit (Abcam, ab176768) according to the manufacturer's instructions. For lipid uptake assays of BODIPY FL C16 (5 µg ml^{-1}; Life Technologies, D3821) and Alexa Fluor 488 AcLDL (5 µg ml^{-1}; Fisher Scientific, 10287482), lipids were added for 3 h at the indicated concentrations and uptake was determined by flow cytometry.

Nuclear extracts and NRF2 activity assay. Cells were washed with ice-cold PBS and resuspended in ice-cold NE Buffer A (10 mM HEPES (pH 7.9), 1.5 mM $MgCl_2$, 10 mM KCl, 1 mM PMSF, 1 µg ml^{-1} leupeptin, 1 µg ml^{-1} aprotinin and 1 mM dithiothreitol). After 5 min of incubation at 4 °C, cells were centrifuged and washed with NE Buffer A three times. After washing, 200 µl of NE Buffer A containing 0.1% NP40 was added. Cells were incubated for 5 min and subsequently centrifuged for 10 min at 4 °C at 9,200*g*. The cytoplasmatic fraction was discarded and the nuclear pellet was resuspended in 75 µl ice-cold NE Buffer C (20 mM HEPES (pH 7.9), 1.5 mM $MgCl_2$, 420 mM NaCl and 25% glycerol). After 15 min of incubation, pellets were centrifuged for 15 min at 16,000*g* at 4 °C and the resulting nuclear fractions frozen at −80 °C. Nrf2 activity of the obtained nuclear fractions was analysed by using the NRF2 activity assay (RayBiotech, TFEM-NRF2-1) according to the manufacturer's instructions.

Metabolic flux measurements. Oxygen consumption rate and ECAR measurements were performed on a Seahorse XFe96 Analyzer (Agilent) using the Seahorse XF Cell Mito Stress test kit (Agilent, 103015-100) according to the manufacturer's instructions. Seahorse plates were coated for 2 h at 37 °C with 40 µl per well of rat tail collagen (Corning, 354236) diluted to 50 mg l^{-1} in milliQ and 0.02 N acetic acid. After coating, wells were washed twice with sterile PBS, and 150,000 peritoneal macrophages were seeded per well in serum-free Agilent Seahorse XF Base medium (Agilent, 103334-100) and pretreated with respective stimuli for the indicated amount of time. During the measurements, oligomycin (1 µM), FCCP (1 µM) and rotenone/antimycin A (500 nM) were subsequently injected. Raw data were analysed using Wave Desktop Software (Agilent, version 2.6.1).

Lipidomics. Regarding serum samples, the lipid extraction was performed as follows: 20 µl of the sample was transferred into a glass vial, and 10 µl internal standard solution (SPLASH Lipidomix, Avanti Polar Lipids) and 140 µl methanol were added. After vortexing, 500 µl methyl tert-butyl ether was added and the mixture was incubated in a shaker for 10 min at room temperature. A phase separation was induced by adding 130 µl MS-grade water. After 10 min of incubation at room temperature, the samples were centrifuged at 1,000*g* for 10 min. A 450-µl aliquot of the upper phase was collected and dried under nitrogen. The samples were reconstituted in 200 µl methanol and used for liquid chromatography–mass spectrometry (LC–MS) analysis. For cell culture samples,

the lipid extraction was performed as follows: the medium was removed, and cells were washed two times with cold PBS. Afterwards, 300 µl of 80% methanol solution was added. After scraping, the cell extract was collected and extraction with 300 µl of 80% methanol solution was repeated. The cell extract was combined and 10 µl of internal standard solution (SPLASH Lipidomix, Avanti Polar Lipids) was added. The cell extract was dried under nitrogen. Then, 150 µl methanol was added to the dry residue. After vortexing, 500 µl methyl tert-butyl ether was added and the mixture was incubated in a shaker for 10 min at room temperature. A phase separation was induced by adding 150 µl MS-grade water. After 10 min of incubation at room temperature, the samples were centrifuged at 1,000*g* for 10 min. An aliquot of 450 µl of the upper phase was collected and dried under nitrogen. The samples were reconstituted in 200 µl methanol and used for LC–MS analysis. The LC–MS analysis was performed using a Vanquish UHPLC system (Thermo Fisher Scientific) combined with an Orbitrap Fusion Lumos Tribrid mass spectrometer (Thermo Fisher Scientific). Lipid separation was performed by reversed-phase chromatography using an Accucore C18, 2.6-µm, 150 × 2 mm (Thermo Fisher Scientific) analytical column at a column temperature of 35 °C. As mobile phase A, an acetonitrile/water (50/50, vol/vol) solution containing 10 mM ammonium formate and 0.1% formic acid was used. Mobile phase B consisted of acetonitrile/isopropanol/water (10/88/2, vol/vol/vol) containing 10 mM ammonium formate and 0.1% formic acid. The flow rate was set to 400 µl min^{-1}. A gradient of mobile phase B was applied to ensure optimal separation of the analysed lipid species. The mass spectrometer was operated in ESI-positive and ESI-negative modes, using the following settings: capillary voltage of 3,500 V (positive) and 3,000 V (negative), vaporize temperature of 320 °C, ion transfer tube temperature of 285 °C, sheath gas of 60 AUs, aux gas of 20 AUs and sweep gas of 1 AU. The Orbitrap MS scan mode at 120,000 mass resolution was used for lipid detection. The scan range was set to 250–1,200 *m/z* for both positive and negative ionization mode. The AGC target was set to 2.0e5 and the intensity threshold to 5.0e3. The data-dependent tandem MS scan using higher-energy collisional dissociation and collision-induced dissociation with fixed collision energy mode set to 35% with an inclusion list was used to obtain tandem MS spectra. The data analysis was performed using the TraceFinder 4.1 software (Thermo Fisher Scientific). Lipid-class-specific isotopically labelled internal standards signal was used to obtain semi-quantitative values for lipids.

Bioinformatics analysis of lipidomics. Lipidomics analysis was performed in Python v.3.7.2. Differences between the addition of ACM or not, were either calculated for all lipids individually, or grouped together to lipid families according to their chemical structure. The changes are depicted as $\log_2$ fold changes between the two conditions, and variance within lipid groups is represented by the s.e.m. Differences in concentrations of lipids in mouse serum among *Pten*^{WT}, *Pten*$^{\Delta myel}$ and *Pten*$^{\Delta myel}$*Marco*$^{-/-}$ are shown as mean normalized abundance of the grouped lipid families. Normalized relative abundance values are calculated by normalizing each individual lipid concentration between the maximum and minimum lipid concentration found within the three conditions, so that the condition with the highest and lowest concentration results in one and zero, respectively. Lipid-to-gene dependencies are illustrated using circus plots[65]. The width of the ribbons corresponds to the percentage of lipids within a lipid family that were significantly upregulated in *Pten*^{WT} with ACM compared to *Pten*^{WT} without ACM (yellow ribbon), *Pten*$^{\Delta myel}$ compared to *Pten*^{WT} (both with ACM; blue ribbon) and between *Pten*$^{\Delta myel}$*Marco*$^{-/-}$ compared to *Pten*^{WT} (both with ACM; red ribbon). Significant upregulation was determined using Student's *t*-test (SciPy v.1.2.0) with a significance threshold of 0.05 and positive fold change. Differences in lipid abundance between FBC and FBC206 ATMs, as well as cellular lipids of *Pten*^{WT} and *Pten*$^{\Delta myel}$ mice, were calculated for lipid families and depicted as *z*-scores using the clustermap function from the Python package seaborn (v.0.9.0). *Z*-scores were calculating using the formula: $z = (x - \mu)/\sigma$, where x is the lipid concentration for one sample, μ is the mean concentration for all samples and σ is the population standard deviation.

Image processing. H&E images of murine livers were acquired using FSX-BSW (02.02, Olympus) software. Images were cropped and processed using Adobe Photoshop CS6, with adjustment for brightness and contrast. Figures were prepared using Adobe Illustrator CS6.

Statistics. Data analysis was performed using Microsoft Excel for Mac 16.41 and Microsoft Excel 2013 (Microsoft Corporation). Statistical analysis was performed using a two-tailed *t*-test for two groups, an ordinary one-way ANOVA followed by Tukey's multiple-comparisons test for multiple groups and a two-way ANOVA followed by Bonferroni's multiple-comparisons test for curve analysis on Prism 8 software (GraphPad), unless stated otherwise. In vitro data are representative of at least two repeats unless stated otherwise, while lipidomics data correspond to biological replicates. Statistical significance is indicated by $^{*}P < 0.05$, $^{**}P < 0.01$, $^{***}P < 0.001$ and $^{****}P < 0.001$. All error bars indicate ± s.e.m.

Reporting Summary. Further information on research design is available in the Nature Research Reporting Summary linked to this article.

Data availability

The data that support the findings of this study are available from the corresponding authors upon request. The lipidomic datasets generated and analysed during the current study are available at https://github.com/menchelab/Marco. Microarray data of Fig. 5a and Extended Data Fig. 4h that support the findings of this study are available in Gene Expression Omnibus under accession number GSE8831 (ref. [10]). Source data are provided with this paper.

Code availability

All code used in the metabolomic differential analyses and subsequent integration is available at https://github.com/menchelab/Marco.

Received: 2 January 2020; Accepted: 9 October 2020;
Published online: 16 November 2020

References

1. Virtue, S. & Vidal-Puig, A. Adipose tissue expandability, lipotoxicity and the Metabolic Syndrome–an allostatic perspective. *Biochim. Biophys. Acta* **1801**, 338–349 (2010).
2. Lackey, D. E. & Olefsky, J. M. Regulation of metabolism by the innate immune system. *Nat. Rev. Endocrinol.* **12**, 15–28 (2016).
3. Russo, L. & Lumeng, C. N. Properties and functions of adipose tissue macrophages in obesity. *Immunology* **155**, 407–417 (2018).
4. Xu, H. et al. Chronic inflammation in fat plays a crucial role in the development of obesity-related insulin resistance. *J. Clin. Invest.* **112**, 1821–1830 (2003).
5. Arkan, M. C. et al. IKK-beta links inflammation to obesity-induced insulin resistance. *Nat. Med.* **11**, 191–198 (2005).
6. Jaitin, D. A. et al. Lipid-associated macrophages control metabolic homeostasis in a Trem2-dependent manner. *Cell* **178**, 686–698 (2019).
7. Hill, D. A. et al. Distinct macrophage populations direct inflammatory versus physiological changes in adipose tissue. *Proc. Natl Acad. Sci. USA* **115**, E5096–E5105 (2018).
8. Li, C. et al. Single-cell transcriptomics based-MacSpectrum reveals novel macrophage activation signatures in diseases. *JCI Insight* **5**, e126453 (2019).
9. Kratz, M. et al. Metabolic dysfunction drives a mechanistically distinct proinflammatory phenotype in adipose tissue macrophages. *Cell Metab.* **20**, 614–625 (2014).
10. Xu, X. et al. Obesity activates a program of lysosomal-dependent lipid metabolism in adipose tissue macrophages independently of classic activation. *Cell Metab.* **18**, 816–830 (2013).
11. Coats, B. R. et al. Metabolically activated adipose tissue macrophages perform detrimental and beneficial functions during diet-induced obesity. *Cell Rep.* **20**, 3149–3161 (2017).
12. Cinti, S. et al. Adipocyte death defines macrophage localization and function in adipose tissue of obese mice and humans. *J. Lipid Res.* **46**, 2347–2355 (2005).
13. Sharif, O., Brunner, J. S., Vogel, A. & Schabbauer, G. Macrophage rewiring by nutrient associated PI3K dependent pathways. *Front Immunol.* **10**, 2002 (2019).
14. Flaherty, S. E. 3rd et al. A lipase-independent pathway of lipid release and immune modulation by adipocytes. *Science* **363**, 989–993 (2019).
15. Boutens, L. et al. Unique metabolic activation of adipose tissue macrophages in obesity promotes inflammatory responses. *Diabetologia* **61**, 942–953 (2018).
16. Saltiel, A. R. & Kahn, C. R. Insulin signalling and the regulation of glucose and lipid metabolism. *Nature* **414**, 799–806 (2001).
17. Winnay, J. N. et al. PI3-kinase mutation linked to insulin and growth factor resistance in vivo. *J. Clin. Invest.* **126**, 1401–1412 (2016).
18. Foukas, L. C. et al. Critical role for the p110α phosphoinositide-3-OH kinase in growth and metabolic regulation. *Nature* **441**, 366–370 (2006).
19. Ciraolo, E. et al. Phosphoinositide 3-kinase p110β activity: key role in metabolism and mammary gland cancer but not development. *Sci. Signal.* **1**, ra3 (2008).
20. Morley, T. S., Xia, J. Y. & Scherer, P. E. Selective enhancement of insulin sensitivity in the mature adipocyte is sufficient for systemic metabolic improvements. *Nat. Commun.* **6**, 7906 (2015).
21. Horie, Y. et al. Hepatocyte-specific *Pten* deficiency results in steatohepatitis and hepatocellular carcinomas. *J. Clin. Invest.* **113**, 1774–1783 (2004).
22. Wijesekara, N. et al. Muscle-specific *Pten* deletion protects against insulin resistance and diabetes. *Mol. Cell. Biol.* **25**, 1135–1145 (2005).
23. Wang, L. et al. Deletion of *Pten* in pancreatic ss-cells protects against deficient β-cell mass and function in mouse models of type 2 diabetes. *Diabetes* **59**, 3117–3126 (2010).
24. Kosteli, A. et al. Weight loss and lipolysis promote a dynamic immune response in murine adipose tissue. *J. Clin. Invest.* **120**, 3466–3479 (2010).
25. Lee, Y. S. et al. Inflammation is necessary for long-term but not short-term high-fat diet-induced insulin resistance. *Diabetes* **60**, 2474–2483 (2011).
26. Ortega-Molina, A. et al. Pten positively regulates brown adipose function, energy expenditure and longevity. *Cell Metab.* **15**, 382–394 (2012).

27. Cucak, H., Grunnet, L. G. & Rosendahl, A. Accumulation of M1-like macrophages in type 2 diabetic islets is followed by a systemic shift in macrophage polarization. *J. Leukoc. Biol.* **95**, 149–160 (2014).
28. Boni-Schnetzler, M. & Meier, D. T. Islet inflammation in type 2 diabetes. *Semin Immunopathol.* **41**, 501–513 (2019).
29. Wang, Y., Viscarra, J., Kim, S. J. & Sul, H. S. Transcriptional regulation of hepatic lipogenesis. *Nat. Rev. Mol. Cell Biol.* **16**, 678–689 (2015).
30. Schabbauer, G. et al. Myeloid PTEN promotes inflammation but impairs bactericidal activities during murine pneumococcal pneumonia. *J. Immunol.* **185**, 468–476 (2010).
31. Wentworth, J. M. et al. Pro-inflammatory $CD11c^{+}CD206^{+}$ adipose tissue macrophages are associated with insulin resistance in human obesity. *Diabetes* **59**, 1648–1656 (2010).
32. Lancaster, G. I. et al. Evidence that TLR4 is not a receptor for saturated fatty acids but mediates lipid-induced inflammation by reprogramming macrophage metabolism. *Cell Metab.* **27**, 1096–1110 (2018).
33. Vangapandu, H. V., Jain, N. & Gandhi, V. Duvelisib: a phosphoinositide-3 kinase δ/γ inhibitor for chronic lymphocytic leukemia. *Expert Opin. Investig. Drugs* **26**, 625–632 (2017).
34. Madisen, L. et al. A robust and high-throughput Cre reporting and characterization system for the whole mouse brain. *Nat. Neurosci.* **13**, 133–140 (2010).
35. Moore, K. J. & Freeman, M. W. Scavenger receptors in atherosclerosis: beyond lipid uptake. *Arterioscler Thromb. Vasc. Biol.* **26**, 1702–1711 (2006).
36. Canton, J., Neculai, D. & Grinstein, S. Scavenger receptors in homeostasis and immunity. *Nat. Rev. Immunol.* **13**, 621–634 (2013).
37. Martin, D. et al. Regulation of heme oxygenase-1 expression through the phosphatidylinositol 3-kinase/Akt pathway and the Nrf2 transcription factor in response to the antioxidant phytochemical carnosol. *J. Biol. Chem.* **279**, 8919–8929 (2004).
38. Ren, D. et al. Brusatol enhances the efficacy of chemotherapy by inhibiting the Nrf2-mediated defense mechanism. *Proc. Natl Acad. Sci. USA* **108**, 1433–1438 (2011).
39. Patrucco, E. et al. PI3Kγ modulates the cardiac response to chronic pressure overload by distinct kinase-dependent and -independent effects. *Cell* **118**, 375–387 (2004).
40. Huang, S. C. et al. Cell-intrinsic lysosomal lipolysis is essential for alternative activation of macrophages. *Nat. Immunol.* **15**, 846–855 (2014).
41. Chavez, J. A. & Summers, S. A. A ceramide-centric view of insulin resistance. *Cell Metab.* **15**, 585–594 (2012).
42. Lumeng, C. N., Bodzin, J. L. & Saltiel, A. R. Obesity induces a phenotypic switch in adipose tissue macrophage polarization. *J. Clin. Invest.* **117**, 175–184 (2007).
43. Fujisaka, S. et al. Regulatory mechanisms for adipose tissue M1 and M2 macrophages in diet-induced obese mice. *Diabetes* **58**, 2574–2582 (2009).
44. Persson, J., Nilsson, J. & Lindholm, M. W. Interleukin-1beta and tumour necrosis factor-alpha impede neutral lipid turnover in macrophage-derived foam cells. *BMC Immunol.* **9**, 70 (2008).
45. Maya-Monteiro, C. M. et al. Leptin induces macrophage lipid body formation by a phosphatidylinositol 3-kinase- and mammalian target of rapamycin-dependent mechanism. *J. Biol. Chem.* **283**, 2203–2210 (2008).
46. Pal, A. et al. *PTEN* mutations as a cause of constitutive insulin sensitivity and obesity. *N. Engl. J. Med.* **367**, 1002–1011 (2012).
47. Dror, E. et al. Postprandial macrophage-derived IL-1β stimulates insulin, and both synergistically promote glucose disposal and inflammation. *Nat. Immunol.* **18**, 283–292 (2017).
48. Mauer, J. et al. Myeloid cell-restricted insulin receptor deficiency protects against obesity-induced inflammation and systemic insulin resistance. *PLoS Genet.* **6**, e1000938 (2010).
49. Ortega-Molina, A. et al. Pharmacological inhibition of PI3K reduces adiposity and metabolic syndrome in obese mice and rhesus monkeys. *Cell Metab.* **21**, 558–570 (2015).
50. Han, S. et al. Macrophage insulin receptor deficiency increases ER stress-induced apoptosis and necrotic core formation in advanced atherosclerotic lesions. *Cell Metab.* **3**, 257–266 (2006).
51. Liang, C. P. et al. Increased CD36 protein as a response to defective insulin signaling in macrophages. *J. Clin. Invest.* **113**, 764–773 (2004).
52. Kzhyshkowska, J., Neyen, C. & Gordon, S. Role of macrophage scavenger receptors in atherosclerosis. *Immunobiology* **217**, 492–502 (2012).
53. Arredouani, M. et al. The scavenger receptor MARCO is required for lung defense against pneumococcal pneumonia and inhaled particles. *J. Exp. Med.* **200**, 267–272 (2004).
54. Dahl, M. et al. Protection against inhaled oxidants through scavenging of oxidized lipids by macrophage receptors MARCO and SR-AI/II. *J. Clin. Invest.* **117**, 757–764 (2007).
55. Yoshimatsu, M. et al. Induction of macrophage scavenger receptor MARCO in nonalcoholic steatohepatitis indicates possible involvement of endotoxin in its pathogenic process. *Int. J. Exp. Pathol.* **85**, 335–343 (2004).
56. Cavallari, J. F. et al. Targeting macrophage scavenger receptor 1 promotes insulin resistance in obese male mice. *Physiol. Rep.* **6**, e13930 (2018).
57. Hirano, S. & Kanno, S. Macrophage receptor with collagenous structure (MARCO) is processed by either macropinocytosis or endocytosis-autophagy pathway. *PLoS ONE* **10**, e0142062 (2015).
58. Rogers, N. J. et al. A defect in *Marco* expression contributes to systemic lupus erythematosus development via failure to clear apoptotic cells. *J. Immunol.* **182**, 1982–1990 (2009).
59. Wermeling, F. et al. Class A scavenger receptors regulate tolerance against apoptotic cells, and autoantibodies against these receptors are predictive of systemic lupus. *J. Exp. Med.* **204**, 2259–2265 (2007).
60. Jung, S. B. et al. Reduced oxidative capacity in macrophages results in systemic insulin resistance. *Nat. Commun.* **9**, 1551 (2018).
61. Mukhopadhyay, S. et al. MARCO, an innate activation marker of macrophages, is a class A scavenger receptor for *Neisseria meningitidis*. *Eur. J. Immunol.* **36**, 940–949 (2006).
62. Itoh, K. et al. An Nrf2/small Maf heterodimer mediates the induction of phase II detoxifying enzyme genes through antioxidant response elements. *Biochem. Biophys. Res. Commun.* **236**, 313–322 (1997).
63. Brandon, A. E. et al. Minimal impact of age and housing temperature on the metabolic phenotype of $Acc2^{-/-}$ mice. *J. Endocrinol.* **228**, 127–134 (2016).
64. Ayala, J. E., Bracy, D. P., McGuinness, O. P. & Wasserman, D. H. Considerations in the design of hyperinsulinemic-euglycemic clamps in the conscious mouse. *Diabetes* **55**, 390–397 (2006).
65. Krzywinski, M. et al. Circos: an information aesthetic for comparative genomics. *Genome Res.* **19**, 1639–1645 (2009).

Acknowledgements

We thank H. Paar, A. Hladik and M. Salzmann for technical assistance. We thank E. Hirsch (Department of Molecular Biotechnology and Health Sciences, Molecular Biotechnology Center, University of Torino) for the $Pi3k\gamma^{KD/KD}$ mice, M. Serrano (IRB Barcelona, Barcelona Institute of Science and Technology) for the $Pten^{Tg/+}$ mice and C. Tsatsanis (Laboratory of Clinical Chemistry, University of Crete Medical School) for the $Akt1^{loxP/loxP}Akt2^{loxP/loxP}LysM\text{-}Cre^{+/-}$ mice. This research was supported by FWF 30026 and 31106 to G.S. and 31568 to O.S. and the Christian Doppler Laboratory for Arginine Metabolism in Rheumatoid Arthritis and Multiple Sclerosis to G.S. J.S.B., A.V. and A.L. were supported by a DOC fellowship of the Austrian Academy of Sciences. A.B. received funding from the European Research Council under the European Union's Seventh Framework Programme and Horizon 2020 research and innovation programme (grant agreement no. 677006; CMIL). M.A.F. is supported by a Senior Principal Research Fellowship from the National Health and Medical Research Council of Australia (APP1116936).

Author contributions

J.S.B., A.V., O.S. and G.S. conceived and designed the study. J.S.B., A.V., A.L., A.K., M.P., M.H., A.H., M. Kieler, L.Q.G., M. Kerndl, M. Kuttke, A.E.B., E.E. and C.L.E. performed experiments. M.C. analysed lipidomic data and performed bioinformatic analysis. I.M. analysed liver steatosis. M.W.G., M. Kulik, P.M.D. and M.S. provided intellectual input. K.K. performed lipidomics analysis. J.S.B., A.V. and A.L. analysed the data. F.G., J.M., A.B., T.W. and M.A.F. provided key resources. J.S.B., A.V., O.S. and G.S. wrote the manuscript. All authors read, revised and approved the final manuscript.

Competing interests

The authors declare no competing interests.

Additional information

Extended data is available for this paper at https://doi.org/10.1038/s42255-020-00311-5.

Supplementary information is available for this paper at https://doi.org/10.1038/s42255-020-00311-5.

Correspondence and requests for materials should be addressed to O.S. or G.S.

Peer review information Primary Handling Editors: Pooja Jha; George Caputa. *Nature Metabolism* thanks Yi-bin Feng and the other, anonymous, reviewer(s) for their contribution to the peer review of this work.

Reprints and permissions information is available at www.nature.com/reprints.

Publisher's note Springer Nature remains neutral with regard to jurisdictional claims in published maps and institutional affiliations.

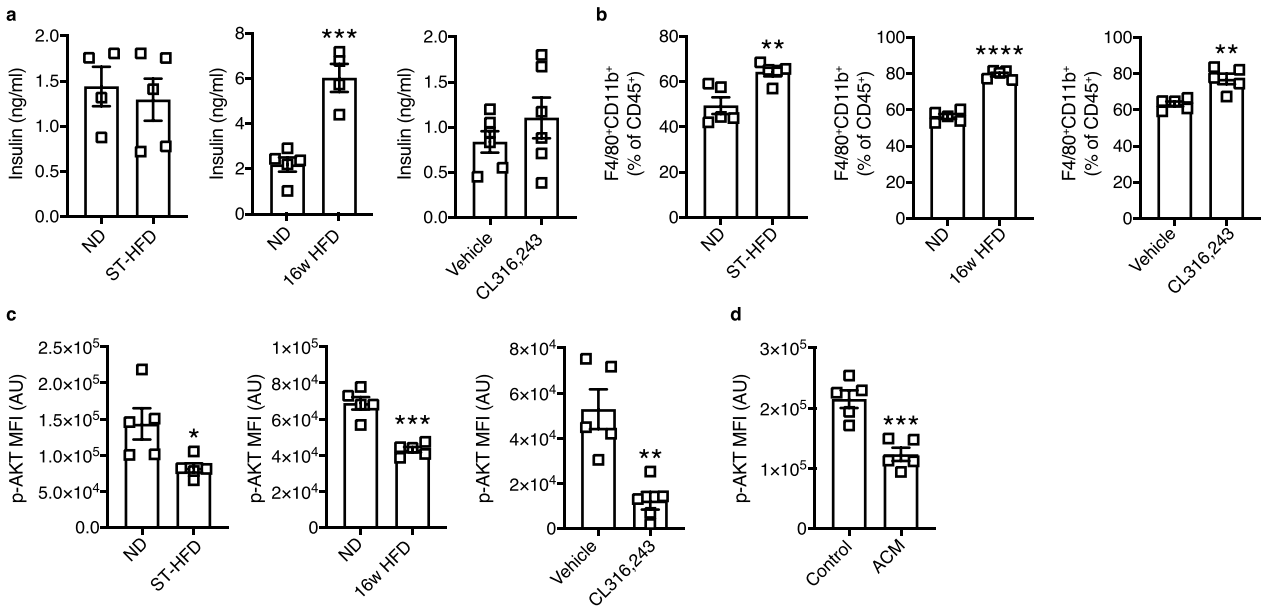

Extended Data Fig. 1 | Disruptions of adipose homeostasis and metabolic stress ablate myeloid PI3K/AKT signalling. a, Serum insulin levels of animals subjected to ST-HFD (n = 4 ND, n = 5 ST-HFD animals), 16 weeks HFD (n = 5 ND, n = 4 HFD animals) or acute lipolysis (n = 6 animals per group) (***P = 0.0006; two-tailed student's t-test). **b**, Percentage of viable FB ($CD45^+CD11b^+F4/80^+$) macrophages and in the adipose tissue of mice post 2 or 16 weeks HFD feeding and acute lipolysis (n = 5 animals; **P = 0.0072, ****P < 0.001, **P = 0.0026; two-tailed student's t-test). **c**, Corresponding p-AKT MFI of FB-ATMs shown in (b) (*P = 0.027, ***P = 0.0001, **P = 0.0029; two-tailed student's t-test). **d**, p-AKT MFI of macrophages post adipocyte conditioned media (ACM) treatment for 3 h (n = 5 samples; ***P = 0.001; two-tailed student's t-test). Data are mean ± SEM and representative of one (a) or two (b-d) independent experiments.

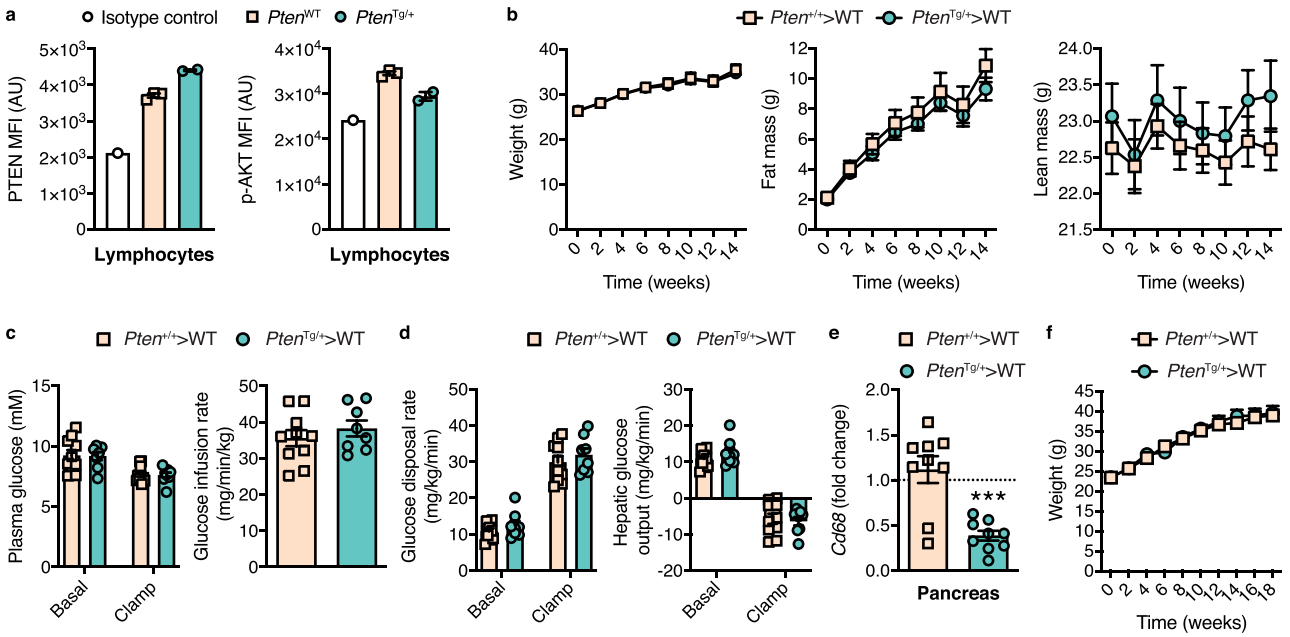

Extended Data Fig. 2 | Adaptive immune cell PTEN and p-AKT, hyperinsulinemic-euglycemic clamps, pancreatic macrophages and weights of BMT animals. a, PTEN and p-AKT expression in adaptive immune cells from blood of WT (n = 3) or *Pten*$^{Tg/+}$ (n = 2) animals. Cells were pre-gated on viable CD45$^+$CD3$^+$B220$^+$. **b**, Weights, fat and lean mass of *Pten*$^{+/+}$>WT (n = 12) or *Pten*$^{Tg/+}$>WT (n = 10) mice as determined using Echo MRI. **c**, Blood glucose levels and glucose infusion rate during clamping of *Pten*$^{+/+}$>WT (n = 10) or *Pten*$^{Tg/+}$>WT (n = 8) mice. **d**, Basal and insulin-stimulated whole-body glucose disposal rates and hepatic glucose production of mice in (**c**). **e**, Pancreatic CD68 expression in *Pten*$^{+/+}$>WT or *Pten*$^{Tg/+}$>WT 16 weeks post HFD (n = 9 animals per genotype; ***P = 0.0003; two-tailed student's t-test). **f**, Weights of mice shown in Fig. 1f-i. Data are mean ± SEM and representative of one (a-e) or two (f) independent experiments.

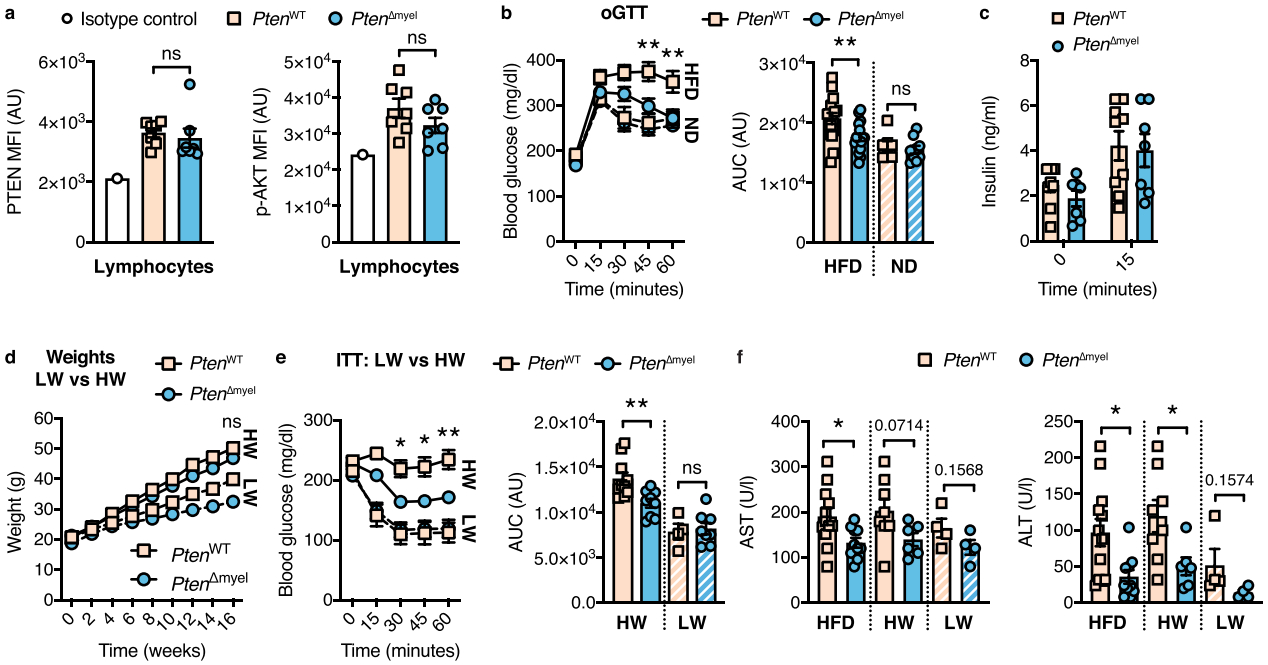

Extended Data Fig. 3 | *In vivo* effects of modulating myeloid PI3K activity are independent of adiposity differences. a, PTEN and p-AKT expression in adaptive immune cells from blood of *Pten*^{WT} (n = 7) or *Pten*$^{\Delta myel}$ (n = 6) mice. Cells were gated on viable CD45$^+$CD3$^+$B220$^+$. Isotype control samples depicted are identical to Extended Data Fig. 2a. **b**, oGTT and AUC of *Pten*^{WT} (n = 7 ND, n = 16 HFD) or *Pten*$^{\Delta myel}$ (n = 9 ND, n = 16 HFD) mice, 16 weeks post feeding (**P = 0.0057, **P = 0.0031; two-way ANOVA, Bonferroni's correction, **P for AUC = 0.009; two-tailed student's t-test). **c**, Serum insulin levels post glucose bolus (n = 9 *Pten*^{WT}, n = 7 *Pten*$^{\Delta myel}$ animals). **d**, Weights of HFD mice shown in Fig. 2b,c stratified for low weight (LW) and high weight (HW) (n = 4 *Pten*^{WT} LW, n = 10 *Pten*^{WT} HW, n = 8 *Pten*$^{\Delta myel}$ LW, n = 9 *Pten*$^{\Delta myel}$ HW). **e**, Insulin tolerance test (ITT) and area under the curve (AUC) post 16 weeks feeding of *Pten*^{WT} (n = 4 LW, n = 10 HW) or *Pten*$^{\Delta myel}$ (n = 8 LW, n = 9 HW) mice stratified for low weight (LW) and high weight (HW) (*P = 0.0216, *P = 0.0151, **P = 0.0037; two-way ANOVA, Bonferroni's correction; **P for AUC = 0.0051; two-tailed student's t-test). **f**, Serum AST and ALT levels post 16 weeks HFD feeding of *Pten*^{WT} (n = 12 HFD, n = 4 LW, n = 8 HW) or *Pten*$^{\Delta myel}$ (n = 10 HFD, n = 4 LW, n = 6 HW) mice stratified for low weight (LW) and high weight (HW) (*P = 0.0185, *P = 0.0126, *P = 0.0293; two-tailed student's t-test). Data are mean ± SEM and representative of one (a, c) or are pooled from two (d-f) or three (b) independent experiments.

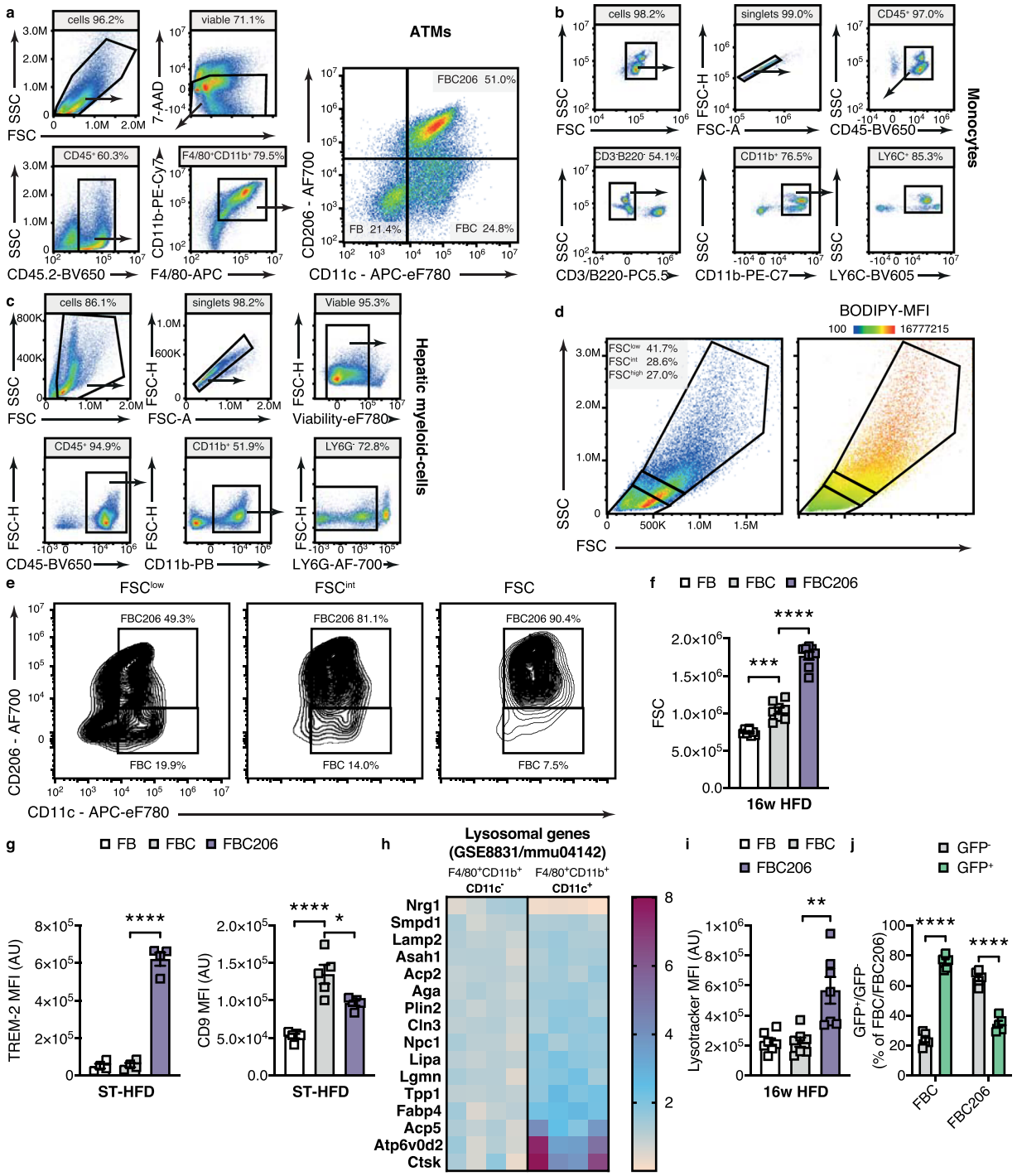

Extended Data Fig. 4 | Gating strategies and FBC206-ATMs are a large, lipid laden, lysotracker, TREM-2^{high} population, mostly of resident origin post ST-HFD. a, Gating strategy of ATMs. **b**, Gating strategy of monocytes. **c**, Gating strategy of hepatic myeloid-cells. **d**, Representative heatmap of BODIPY MFI in relation to cell size (FSC) of cells isolated from eWAT post 16 weeks HFD. **e**, Representative percentages of FBC and FBC206 populations within FSC low, intermediate and high low cells are depicted. Cells were pre-gated on live CD45$^+$CD11b$^+$F4/80$^+$. **f**, Cell size quantification according to forward scatter (FSC) of FB-, FBC- and FBC206-ATMs (n = 8 animals; ***P = 0.0001, ****P < 0.0001; one-way ANOVA, Bonferroni's correction). **g**, TREM-2 and CD9 MFI of FB-, FBC- and FBC206-ATMs post ST-HFD (n = 5 animals; ****P < 0.0001, *P = 0.013; one-way ANOVA, Bonferroni's correction). **h**, Lysosomal gene expression based on KEGG pathway (mmu04142) of microarray data of obese FBs vs FBCs from C57Bl/6 J Lep$^{ob/ob}$ mice (GSE8831). Data depicted as fold change relative to FB condition. **i**, Lysotracker MFI of the FBC206-ATM population post 16 weeks HFD (n = 7 animals; **P = 0.011; one-way ANOVA, Bonferroni's correction). **j**, Post ST-HFD, percentages of GFP$^-$ FBC- vs GFP$^+$ FBC-ATMs and GFP$^-$ FBC206- vs GFP$^+$ FBC206-ATMs were analysed in eWAT of *Ccr2*$^{GFP/+}$ animals. Cells were pre-gated on CD45$^+$CD11b$^+$F4/80$^+$ (n = 5 animals; ****P < 0.0001; two-way ANOVA, Bonferroni's correction). Data are mean ± SEM and representative of one (g, i), two (j) or four (d-f) independent experiments.

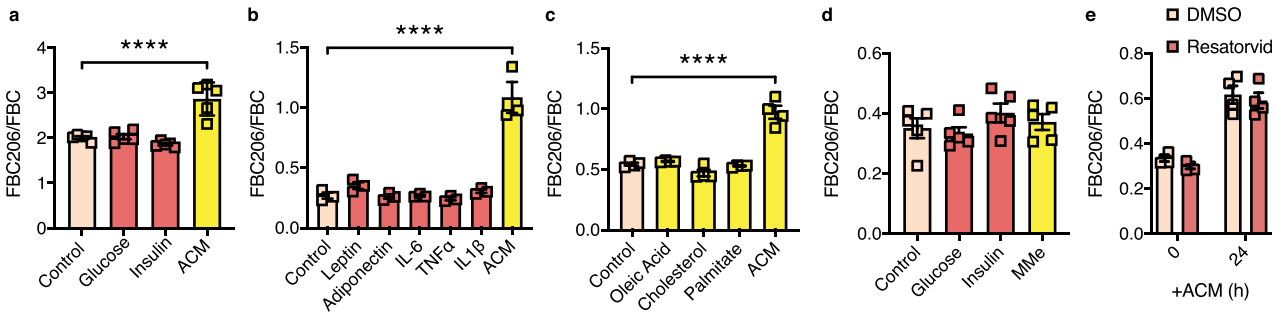

Extended Data Fig. 5 | FBC206 generation of naïve macrophages stimulated with the indicated cytokines, adipokines and lipids. a, FBC206/FBC ratio of macrophages post stimulation with glucose, insulin and ACM for 24 hours (n = 5 samples; ****P < 0.0001; one-way ANOVA, Bonferroni's correction). **b**, FBC206/FBC ratio of macrophages post stimulation with various cytokines and ACM for 24 hours (n = 3 samples; ****P < 0.0001; one-way ANOVA, Bonferroni's correction). **c**, FBC206/FBC ratio of macrophages post stimulation with various lipids and ACM for 24 hours (n = 4 samples; ****P < 0.0001; one-way ANOVA, Bonferroni's correction). **d**, FBC206/FBC ratio of macrophages post stimulation with glucose, insulin and MMe for 24 hours (n = 5 samples). **e**, FBC206/FBC ratio and BODIPY MFI of naïve macrophages treated with Resatorvid and ACM for 24 hours (n = 4 samples). Data are mean ± SEM and representative of two (a-e) independent experiments.

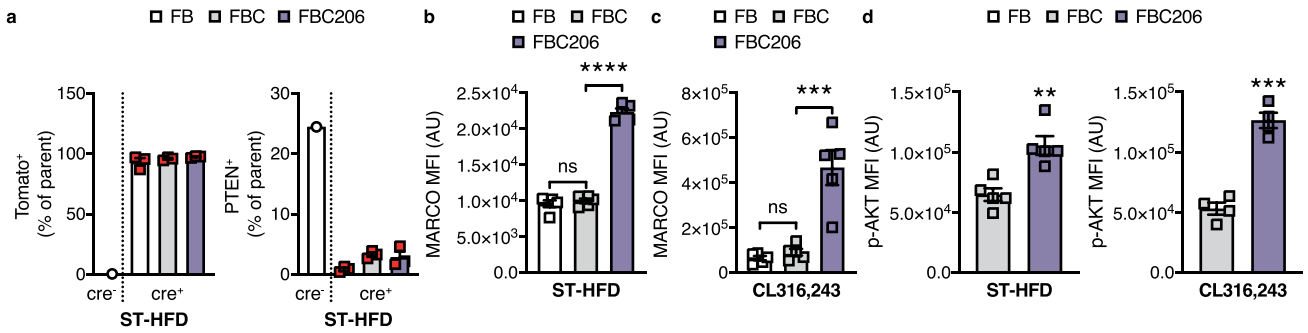

Extended Data Fig. 6 | MARCO and p-AKT post ST-HFD and acute lipolysis in the different ATM populations, where PTEN is deleted equally. **a**, Percentages of Tomato$^+$ and PTEN$^+$ ATMs represented as percentage of their respective parent (FB-, FBC- or FBC206-ATMs) post ST-HFD in *Pten*^{WT}R26^{tdTomato} (cre$^-$) and *Pten*$^{\Delta myel}$R26^{tdTomato} (cre$^+$) mice (n = 3 animals). **b/c**, MARCO MFI in macrophages post ST-HFD (b) or acute lipolysis (c). Cells were pre-gated on viable FBs (CD45$^+$CD11b$^+$F4/80$^+$) (n = 5 animals; ****P < 0.0001, ***P = 0.0003; one-way ANOVA, Bonferroni's correction). **d**, p-AKT MFI of FBC- and FBC206-ATMs of mice post ST-HFD or after acute lipolysis (n = 5 ST-HFD, n = 4 CL316,243 animals; **P = 0.0025, ***P = 0.0001; two-tailed student's t-test). Data are mean ± SEM and representative of one (a) or two (b-d) independent experiments.

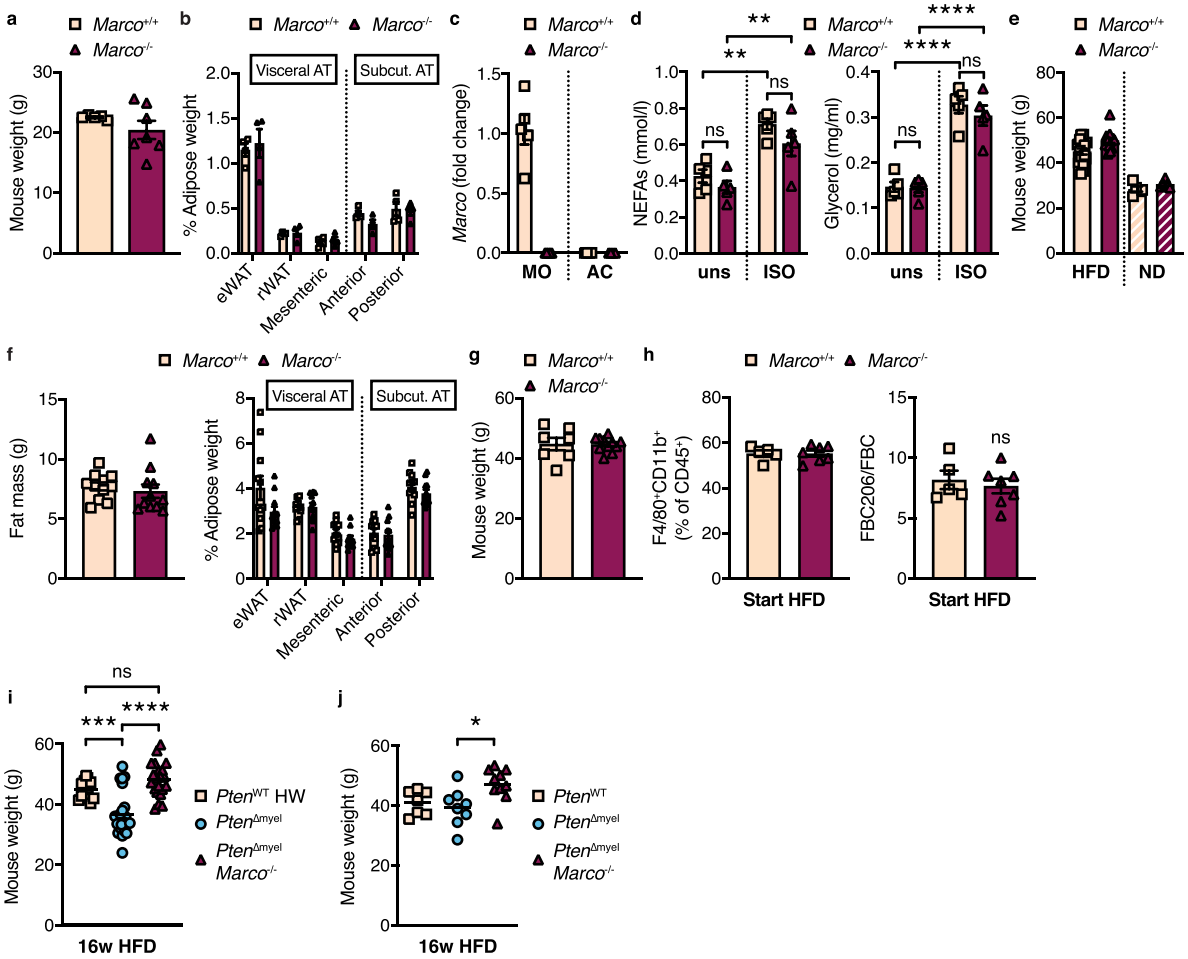

Extended Data Fig. 7 | Impaired lipid buffering of *Marco*$^{-/-}$ mice is not associated with adiposity differences and weights of animals in Fig. 8d,e. **a**, Weight of mice in Fig. 6c. **b**, Fat depot distribution of lean *Marco*$^{+/+}$ and *Marco*^{n} mice presented as percent of bodyweight (n = 4 mice per genotype). RP: retroperitoneal, eWAT: epididymal, VAT: visceral, SAT: subcutaneous, white adipose tissue depots. **c**, *Marco* transcript levels measured in macrophages (n = 5 samples) and adipocytes (n = 4 samples). **d**, NEFA and glycerol levels of adipose tissue isolated from lean *Marco*$^{+/+}$ and *Marco*$^{-/-}$ mice, stimulated with isoproterenol (ISO) for 2 hours (n = 5 animals; **P = 0.0022, **P = 0.0099, ****P < 0.0001; one-way ANOVA, Bonferroni's correction). **e**, Weight of mice in Fig. 6d. **f**, Fat mass and adipose depot distribution of *Marco*$^{+/+}$ and *Marco*$^{-/-}$ mice post 16 weeks HFD. RP: retroperitoneal, eWAT: epididymal, VAT: visceral, SAT: subcutaneous, white adipose tissue depots (n = 11 mice per genotype). **g**, Weights of mice shown in Fig. 6e. **h**, Macrophage content and FBC206/FBC ratios of *Marco*$^{+/+}$ (n = 5) and *Marco*$^{-/-}$ (n = 7) mice prior to HFD feeding. **i**, Corresponding weights of mice in Fig. 8d (***P = 0.0009, ****P < 0.0001; one-way ANOVA, Bonferroni's correction). **j**, Corresponding weights of mice in Fig. 8e (*P = 0.0181; one-way ANOVA, Bonferroni's correction). Data are mean ± SEM and representative of one (b, c, g, h), two (a, d), or are pooled from two (f, j), four (e) or six (i) independent experiments.

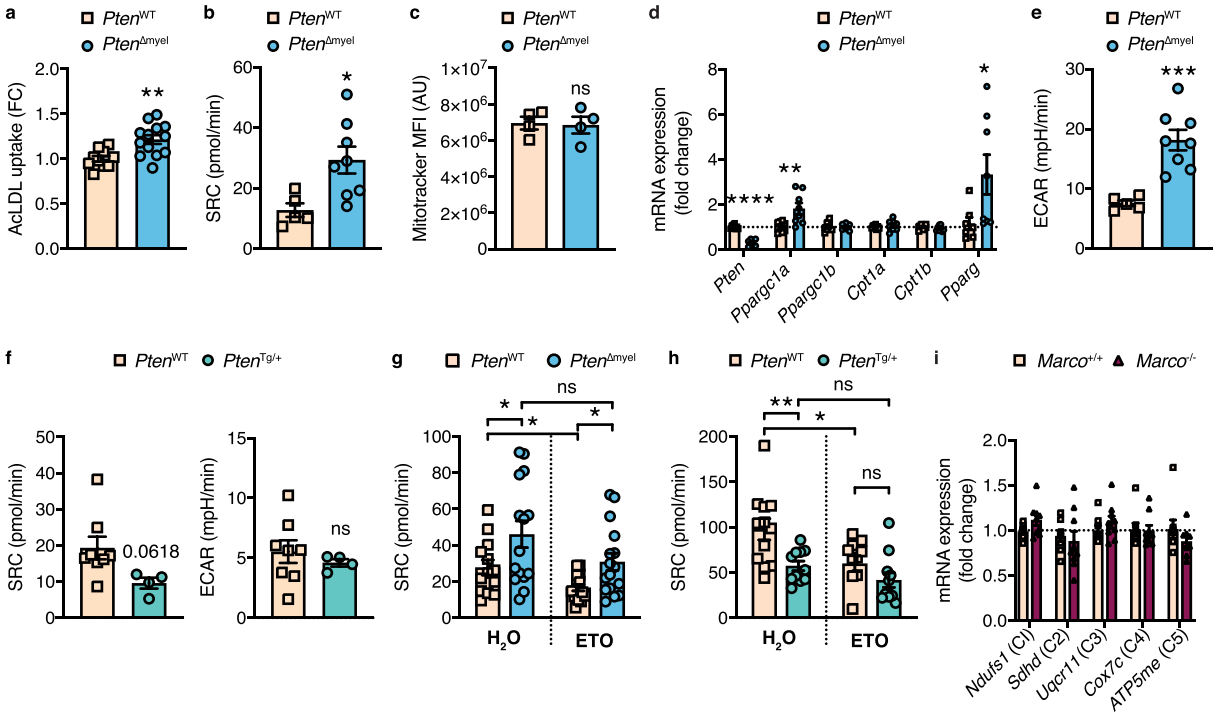

Extended Data Fig. 8 | PI3K-dependent differences in lipid uptake and catabolism are independent of mitochondrial numbers and mitochondrial respiratory chain complex expression of *Marco*$^{-/-}$ macrophages. a, AcLDL uptake of naïve macrophages from *Pten*^{WT} (n = 10) and *Pten*$^{\Delta myel}$ (n = 13) mice depicted as fold change (FC) increase (**P = 0.0025; two-tailed student's t-test). **b**, Spare respiratory capacity (SRC) of data in Fig. 7e (*P = 0.0184; two-tailed student's t-test). **c**, Mitochondrial numbers in naïve *Pten*^{WT} and *Pten*$^{\Delta myel}$ macrophages as determined using Mitotracker (n = 4 samples per genotype). **d**, mRNA levels of *Pten* and selected mitochondrial marker genes in naïve *Pten*^{WT} (n = 8, for *Pparg* n = 7 samples) and *Pten*$^{\Delta myel}$ (n = 8 samples) macrophages (****P < 0.0001, **P = 0.0091, *P = 0.443; two-tailed student's t-test). **e**, Extracellular acidification rate (ECAR) of data in Fig. 7e (***P = 0.0007; two-tailed student's t-test). **f**, SRC and ECAR of data in Fig. 7f (two-tailed student's t-test). **g**, SRC of data in Fig. 7g (*P = 0.0487, *P = 0.0173, *P = 0.0111; two-tailed student's t-test). **h**, SRC of data in Fig. 7h (**P = 0.0063, *P = 0.0171; two-tailed student's t-test). **i**, mRNA levels of selected mitochondrial complex genes in naïve *Marco*$^{+/+}$ (n = 8 samples) and *Marco*$^{-/-}$ (n = 9 samples) macrophages. The mitochondrial complex (C) represented by each gene is indicated. Data are mean ± SEM and representative of two (b-h), or are pooled from two (a, i) independent experiments.

nature research

Corresponding author(s): Sharif O. & Schabbauer G.

Last updated by author(s): Sep 28, 2020

Reporting Summary

Nature Research wishes to improve the reproducibility of the work that we publish. This form provides structure for consistency and transparency in reporting. For further information on Nature Research policies, see Authors & Referees and the Editorial Policy Checklist.

Statistics

For all statistical analyses, confirm that the following items are present in the figure legend, table legend, main text, or Methods section.

n/a	Confirmed
☐	☒ The exact sample size (*n*) for each experimental group/condition, given as a discrete number and unit of measurement
☐	☒ A statement on whether measurements were taken from distinct samples or whether the same sample was measured repeatedly
☐	☒ The statistical test(s) used AND whether they are one- or two-sided *Only common tests should be described solely by name; describe more complex techniques in the Methods section.*
☐	☒ A description of all covariates tested
☐	☒ A description of any assumptions or corrections, such as tests of normality and adjustment for multiple comparisons
☐	☒ A full description of the statistical parameters including central tendency (e.g. means) or other basic estimates (e.g. regression coefficient) AND variation (e.g. standard deviation) or associated estimates of uncertainty (e.g. confidence intervals)
☐	☒ For null hypothesis testing, the test statistic (e.g. *F*, *t*, *r*) with confidence intervals, effect sizes, degrees of freedom and *P* value noted *Give P values as exact values whenever suitable.*
☒	☐ For Bayesian analysis, information on the choice of priors and Markov chain Monte Carlo settings
☒	☐ For hierarchical and complex designs, identification of the appropriate level for tests and full reporting of outcomes
☒	☐ Estimates of effect sizes (e.g. Cohen's *d*, Pearson's *r*), indicating how they were calculated

Our web collection on statistics for biologists contains articles on many of the points above.

Software and code

Policy information about availability of computer code

Data collection	Step-OnePlus Real-Time PCR Software v2.3; Gen5 1.11; Wave Desktop Software 2.6.1.; CytExpert 2.3; FSX-BSW(02.02); GitHub (https://github.com/menchelab/Marco)
Data analysis	Microsoft Excel for Mac 16.41 and Microsoft Excel 2013; TraceFinder 4.1 software; FlowJo 10; CytExpert 2.3; Prism 8; Adobe Illustrator CS6; Adobe Photoshop CS6; Python v. 3.7.2; SciPy v. 1.2.0; Circos v. 0.69-3; numpy v. 1.16.0; pandas v. 0.24.0; sklearn v. 0.20.3; matplotlib v. 3.0.2; statsmodels v. 0.10.1; seaborn v. 0.9.0

For manuscripts utilizing custom algorithms or software that are central to the research but not yet described in published literature, software must be made available to editors/reviewers. We strongly encourage code deposition in a community repository (e.g. GitHub). See the Nature Research guidelines for submitting code & software for further information.

Data

Policy information about availability of data

All manuscripts must include a data availability statement. This statement should provide the following information, where applicable:

- Accession codes, unique identifiers, or web links for publicly available datasets
- A list of figures that have associated raw data
- A description of any restrictions on data availability

The data that support the findings of this study are available from the corresponding authors upon reasonable request. Lipidomics raw data is available on GitHub (https://github.com/menchelab/Marco). Data that support the findings of this study are available in Gene Expression Omnibus (GEO) under accession number GSE8831.

Field-specific reporting

Please select the one below that is the best fit for your research. If you are not sure, read the appropriate sections before making your selection.

☒ Life sciences ☐ Behavioural & social sciences ☐ Ecological, evolutionary & environmental sciences

For a reference copy of the document with all sections, see nature.com/documents/nr-reporting-summary-flat.pdf

Life sciences study design

All studies must disclose on these points even when the disclosure is negative.

Sample size	Sample size calculations were based on effect size with a power=0.8 and alpha level=0.05 and were based on previous experience. Sample sizes for animal experiments was approved by the local ethics committee. Please see Frommlet & Heinze, 2020 (https://doi.org/10.1177/0023677220907617).
Data exclusions	No data except statistical significant outliers were excluded in this study. Statistical outliers have been excluded based on alpha=0.05 on Prism 8 software using Grubbs' Outlier Test (GraphPad, La Jolla, CA). No other exclusion criteria were established or applied.
Replication	All experiments were performed at least two times and represent reproducible findings, except stated otherwise. If possible, we usually use at least three independent biological replicates. Lipidomics data represent single experiments using biological replicates, showed low sample variation and were verified using complementary in vitro approaches.
Randomization	Mice were grouped randomly per cage.
Blinding	Steatosis scores were recorded by a blinded, experienced pathologist. For most other experiments the investigators were not blinded to group allocations.

Reporting for specific materials, systems and methods

We require information from authors about some types of materials, experimental systems and methods used in many studies. Here, indicate whether each material, system or method listed is relevant to your study. If you are not sure if a list item applies to your research, read the appropriate section before selecting a response.

Materials & experimental systems

n/a	Involved in the study
☐	☒ Antibodies
☒	☐ Eukaryotic cell lines
☒	☐ Palaeontology
☐	☒ Animals and other organisms
☒	☐ Human research participants
☒	☐ Clinical data

Methods

n/a	Involved in the study
☒	☐ ChIP-seq
☐	☒ Flow cytometry
☒	☐ MRI-based neuroimaging

Antibodies

Antibodies used	The following antibodies were used: CD45.2-BV650 (Clone 104, BioLegend #109836, 1:100), CD45-V500 (Clone 30-F11, BD Horizon #561487, 1:100), F4/80-BV605 (Clone BM8, BioLegend #123133, 1:80), F4/80-FITC (Clone BM8, BioLegend #123108, 1:100), CD11b-PeCy7 (Clone M1/70, eBioscience #25-0112, 1:500), CD11b-PB (Clone M1/70, Invitrogen #RM2828, 1:100), CD11c-APC-eF780 (Clone N418, eBioscience #47-0114, 1:100), CD11c-PC5.5 (Clone N418, eBioscience #35-0114-82, 1:80), CD206-AF700 (Clone C068C2, BioLegend #141733, 1:200), CD206-PE (Clone C068C2, BioLegend #141705, 1:100), MARCO-APC (Clone 579511, R&D #FAB2956A, 1:25), MARCO-PE (Clone ED31, Invitrogen #15225929, 1:50), CD9-PE (Clone MZ3, BioLegend #124805, 1:200), TREM2-PE (Clone 237920, R&D #FAB17291P, 1:15), Ly6G-AF700 (Clone 1A8, BioLegend #127622, 1:200), Ly6C-BV605 (Clone HK1.4, BioLegend #128035, 1:80), Ly6C-PE/Cy7 (Clone HK1.4, BioLegend #128017, 1:100), B220-PE-Cy5 (Clone RA3-6B2, Tonbo #55-0452, 1:80), CD3-PerCP-Cy5.5 (Clone 145-2C11, Tonbo #65-0031, 1:80), CD3-APC (Clone 17A2, eBioscience #17-0032-82, 1:160), CD19-BV605 (Clone 6D5, BioLegend #115540, 1:200), CD4-AF700 (Clone RM4-5, eBioscience #56-0042-82, 1:100), CD8-Pe/Cy7 (Clone 53-6.7, BioLegend #100721, 1:200). Intracellular staining was performed by using the fixation and permeabilization buffer set (eBioscience #88-8824-00) or True-Phos Buffer Set (Biolegend #425401) according to the manufacturer's instruction and included p-AKT-APC (Clone SDRNR, eBioscience #17-9715-42, 1:50) and PTEN-BV421 (Clone A2B1, BD #566637, 1:30) or isotype controls mouse IgG2a-APC (Clone eBM2a, eBioscience #17-4724-81, 1:50) and mouse IgG1k-BV421 (Clone X40, BD #562438, 1:30).
Validation	All antibody are commercially available and their validation statements are available on the manufacturer's website. All antibodies were validated as per manufacturer instruction. For FACS antibodies unstained control, single stainings and fluorescent minus one stainings were included to control for auto-fluorescence and over- or undercompensation.

Animals and other organisms

Policy information about studies involving animals; ARRIVE guidelines recommended for reporting animal research

Laboratory animals	Mice were bred and housed in pathogen-free facilities at the Medical University of Vienna and were kept in a 12 hour light cycle, 21-23°C temperature and 45-65% humidity in cages with maximum 4 male and 5 female animals per cage. Wildtypes were on the C57BL/6J background and purchased from Charles River Laboratories (JAX™ Mice Strain, Code #632). PtenloxP/loxPLysMCre +/- (MGI ID 2182005 and 1934631, PtenDmyel) mice were backcrossed to a C57BL/6J background for at least eight generations. For deletion efficiency experiments, PtenDmyel were further crossed to R26tdTomato mice (C57BL/6J background, MGI ID 3813512), which were a kind gift from Christoph Österreicher. PtenTg/+ mice (MGI ID 5645732) on a C57BL6/CBA background were supplied by the M. Serrano Lab and bred with C57BL/6J females (at least for 5 generations). Resulting male 8-12 week old mice were used as donors for bone marrow transplantations. Marco-/- mice (C57BL/6 background, MGI: 1309998) were backcrossed for at least 5 generation to a C57BL/6J background and were a kind gift from K. Tryggvason. PtenDmyel and Marco-/- were in house inter-crossed to generate Pten and Marco double deficient mice (PtenDmyelMarco-/-). Nrf2-/- mice (C57BL/6 background, Riken BRC #RBRC01390) were kindly provided by Masayuki Yamamoto and Florian Gruber. Ccr2gfp/gfp mice were bought from the Jackson Laboratories (#027619). PI3KgKD/KD (C57BL/6J background, MGI ID 3051886) mice were kindly provided by Emilio Hirsch. Akt1loxP/loxPAkt2loxP/loxPLysMCre+/- mice (C57BL/6J background, Jackson Laboratory #026474 #026475) were a kind gift from Christos Tsatsanis. Eight to twelve weeks old sex and age-matched littermates were used for in vitro approaches. For in vivo experiments male, eight to twelve weeks old, age-matched mice and their respective littermate controls were used unless otherwise stated. Mice were maintained on a normal chow diet (#V1536 Ssniff). Dietary interventions commenced at 6 weeks of age using a diet that contained 60% calories from fat (Research Diets, #D12492) or in the case of normal diet studies, mice were maintained on the chow diet (Ssniff #V1536).
Wild animals	No wild animals were used in this study.
Field-collected samples	No field collected samples were used in this study.
Ethics oversight	All experimental procedures were approved by the Austrian Ministry of Sciences under the project numbers 66.009/0066-WF/V/3b/2016, 66.009/0097-WF/V/3b/2017, 66.009/0377-V/3b/2019 and 66.009/0264-V/3b/2019 and were conducted in strict accordance with Austrian law. Animal experiments performed in Australia were granted permission under project number 17-04 at the Garvan and St. Vincent's Ethics Committee, NSW, Australia.

Note that full information on the approval of the study protocol must also be provided in the manuscript.

Flow Cytometry

Plots

Confirm that:

☒ The axis labels state the marker and fluorochrome used (e.g. CD4-FITC).

☒ The axis scales are clearly visible. Include numbers along axes only for bottom left plot of group (a 'group' is an analysis of identical markers).

☒ All plots are contour plots with outliers or pseudocolor plots.

☒ A numerical value for number of cells or percentage (with statistics) is provided.

Methodology

Sample preparation	Regarding peritoneal macrophage isolation, animals were sacrificed by cervical dislocation and their peritoneal cavity was flushed with sterile 1x PBS. Cells were plated, washed after 3 hours and supplemented with complete RPMI medium. On the following day, cells were stimulated as indicated. For flow cytometry, cells were detached using Enzyme Free (Milipore #S-014-B) and subsequently stained. Regarding immune cell isolation, epididymal fat pads were harvested from indicated animals, cut into small pieces and washed twice with DMEM:F12 media (Gibco, #11320-074) followed by centrifugation for 8 min at 1,800 rpm at room temperature. Digestion was carried out in 10 mL of freshly prepared collagenase II solution (1 mg/mL in 1.5% sterile BSA, in DMEM:F12) at 37° C for 1 hour. Subsequently, 100 µL of 0.5M EDTA was added and the digested adipose-enzyme solution was filtered through a 100 µm strainer into 20 mL DMEM:F12 media supplemented with 10% FBS and centrifuged as previously. Post centrifugation, the pellet was washed twice and resuspended in 1 mL of erythrocyte lysis buffer (Qiagen #79217) for 5 min, after which 12 mL of media was added. The resulting cell suspension was counted, centrifuged and further stained for flow cytometric analysis. For cell sorting, murine ATMs were filtered through a 40 µM cell strainer and sorted as live, CD45+CD3-CD11b+F4/80+CD11c+CD206 +/- on a FACSAria™ II flow cytometer (BD). Isolation of liver mononuclear cells was performed as previously described. Briefly, via the portal vein, livers were perfused with HBSS, cut into small pieces and digested in RPMI containing 0.05% collagenase/dispase (Roche #10269638001) and 0.01% trypsin inhibitor (Thermo Fisher Scientific #17075029) for 1 hr at 37°C. The resulting liver suspension was passed through a 40 µm cell strainer, centrifuged at 800 g (10 min, 4°C) and the cell pellet was resuspended in 10 ml RPMI. Cell suspensions were overlayed onto 15 ml of 33% (Vol/Vol) Percoll solution (Sigma-Aldrich #P1644) and centrifuged for 30 min at room temperature with no brake. The supernatant was removed and erythrocytes were lysed by resuspending the pellet in 2 ml of red blood cell lysis buffer for 4 min, after which 8 ml of RPMI was added. Cell suspensions were spun at 800 g (5-10 min, 4°C), supernatant removed and the cells were washed twice with 10 ml RPMI. Cells were subsequently resuspended in PBS/2%FBS and total cell numbers per liver were enumerated using a haemocytometer (Turck chamber) before staining for flow cytometry. For flow cytometric analysis of blood monocytes, EDTA-blood was stained with antibodies and subsequently fixed with 2% PFA

	for 15 min. The cell suspension was further subjected to red blood cell lysis prior to processing for intracellular staining or flow cytometric analysis.
Instrument	CytoFLEX S Flow Cytometry (Beckman Coulter), FACSAria™ II flow cytometer (BD)
Software	CytExpert (Version 2.0) and FlowJo (Version 10, LLC) software
Cell population abundance	Post peritoneal macrophage detachment, a minimum of 10,000 live macrophages were recorded per sample. Post sample harvest from tissue and blood, a minimum 50,000 live immune cells were recorded per sample.
Gating strategy	Cells were gated on FSC-A/SSC-A. Where appropriate, cells were gated on live using fixable viability dye (Invitrogen #65-0865-14). A detailed gating strategy is provided in Extended Data Fig. 4a-c.

☒ Tick this box to confirm that a figure exemplifying the gating strategy is provided in the Supplementary Information.